Department of Precision and Microsystems Engineering

Topology Optimization of Geometrically Nonlinear Structures

B. P. F. Holtzer

Report no : 2017.024
Coach : Prof. dr. ir. F. van Keulen
Professor : Prof. dr. ir. F. van Keulen
Specialisation : Engineering Mechanics
Type of report : Master Thesis
Date : July 12, 2017

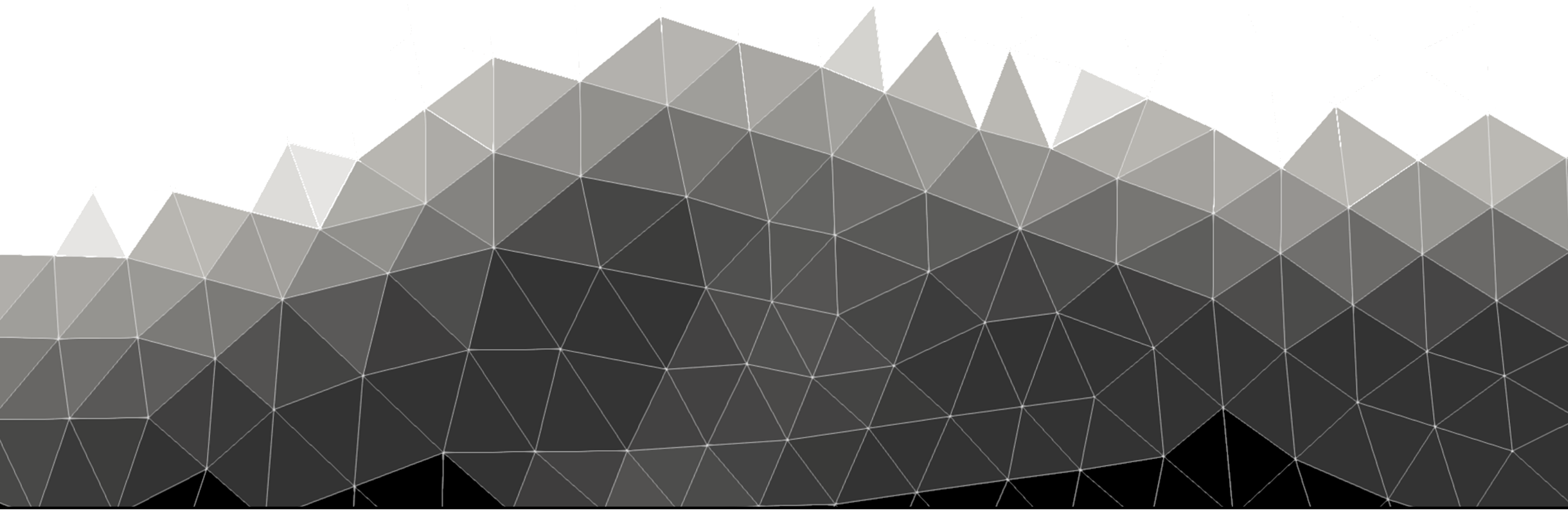

TUDelft Delft University of Technology

Challenge the future

TOPOLOGY OPTIMIZATION OF GEOMETRICALLY NONLINEAR STRUCTURES

DEPARTMENT OF PRECISION AND MICROSYSTEMS ENGINEERING

by

B. P. F. Holtzer

in partial fulfillment of the requirements for the degree of

Master of Science
in Mechanical Engineering

at the Delft University of Technology,
to be defended publicly on July 12, 2017 at 12:45.

Student number:	4138929	
Project duration:	September 1, 2016 – July 12, 2017	
Supervisor:	Prof. dr. ir. F. van Keulen	
Thesis committee:	Prof. dr. ir. F. van Keulen,	TU Delft
	Dr. ir. A. M. Aragón,	TU Delft
	Dr. ir. R. A. J. van Ostayen,	TU Delft
	Dr. ir. S. Turteltaub,	TU Delft

TUDelft Delft University of Technology

ABSTRACT

So far, structural topology optimization has been mainly focused on linear problems. Much less attention has been paid to geometrically nonlinear problems, although it has a lot of interesting applications. The objective of this work is to implement a method to solve topology optimization problems under finite displacements and rotations. The main focus is on designing stiff structures, but also an outlook is presented on the design of structures that follow a prescribed equilibrium path.

The Newton-Raphson incremental-iterative procedure is implemented to solve nonlinear problems. Arc-length control is used to be able to overcome limit points and to obtain faster convergence. It is shown by means of numerical experiments that this method leads to correct results.

Since nonlinear analysis, especially in combination with topology optimization, is computationally expensive, an attempt is made to develop a new reduction method. This method uses load dependent Ritz vectors as a reduced basis and was originally used in linear dynamic problems. However, it is demonstrated that this method will in general not lead to accurate results in nonlinear static problems. This is due to the fact that deformation modes that are not excited by the external force, cannot be described by the basis.

The topology optimization process is implemented without reduction method. An adjoint formulation is derived to obtain sensitivities in a computationally efficient way. By means of several examples of end-compliance minimization, it is demonstrated that in most cases, especially for shell structures, this method leads to better performing designs than topology optimization based on linear analysis.

PREFACE

This report is not only the conclusion of my Master Thesis, but also of my studies mechanical engineering in Delft. It combines the two subjects of mechanical engineering I like most, namely: nonlinear mechanics and topology optimization. I liked studying the fundamentals of mechanics and implementing a method to analyze these problems numerically. In addition, I was very much intrigued how topology optimization can automate a design process. Also programming in Python became fun when I managed to get the code working.

I would like to thank my supervisor Prof. dr. ir. F. van Keulen for all the fun discussions we had during my progress meetings. Also, I want to thank Max and Thijs for helping me learn the Python programming language and understand the working of hybrida. I also very much enjoyed the discussions in the office, and all the delicious dinners we had together. This made graduating a beautiful year never to forget. Last but not least, I want to thank Susan, for always supporting me.

B. P. F. Holtzer
Delft, July, 2017

NOMENCLATURE

In this work, a lower-and upper-case letter represents a scalar, a lower-case bold letter represents a vector and an upper-case bold letter represents a matrix.

$\mathbf{A}$	Filter matrix
A	Area, Cross-sectional area
$\mathbf{a}$	Derivative of constraint equation with respect to nodal displacements
$\mathbf{B}$	Strain-displacement matrix
B	Width
C	(End-)compliance
c	Constraint equation
$\mathbf{D}$	Constitutive (stiffness) matrix
E	Young's modulus
e	Element number
$\mathbf{f}$	Nodal force vector
f	Objective function
$\mathbf{G}$	Matrix containing spatial derivatives of shape functions
g	Derivative of constraint equation with respect to load parameter
H	Height
h	Thickness
$\mathbf{I}$	Identity matrix
j	Iteration number
$\mathbf{K}$	Tangent stiffness matrix
$\mathbf{K}_{\mathrm{M}}$	Material or physical stiffness matrix
$\mathbf{K}_{\mathrm{G}}$	Geometric stiffness matrix
k	Spring stiffness
L	Length
l	Arc-length or step size
$\mathbf{l}$	Selection vector
$\mathbf{M}$	Mass matrix
N	Number of iterations, size of the full system
n	Size of the reduced system
P	Applied force
p	Penalization parameter
$\mathbf{q}$	Modal load vector
R	Radius
$\mathbf{r}$	Residual nodal force vector
$\mathbf{S}$	Matrix containing second Piola-Kirchhoff stress components
t	Pseudo-time
$\mathbf{u}$	Nodal displacement vector
$\mathbf{V}$	Load dependent Ritz vector basis
V	Volume
$\mathbf{v}$	Load dependent Ritz vector
W	Work
$\mathbf{w}$	Buckling mode

w	Weight factor
x	First cartesian coordinate
y	Second cartesian coordinate
z	Third cartesian coordinate

α	Weight factor
β	Load scaling parameter in arc-length control
γ	Arc-length amplification parameter
Δ	Incremental difference operator
δ	Iterative difference operator, variational operator
$\boldsymbol{\varepsilon}$	Green-Lagrange deformation vector
ζ	Triangular coordinate
θ	Angle cylindrical roof
$\boldsymbol{\kappa}$	Modal stiffness matrix
κ	Modal stiffness
λ	Load parameter
$\boldsymbol{\mu}$	Adjoint variables or Lagrange multipliers
ν	Poisson's ratio
Π	Potential energy
ρ	Element density
$\boldsymbol{\sigma}$	Second Piola-Kirchhoff stress vector
$\boldsymbol{\Phi}$	Modal matrix containing all eigenvectors
$\boldsymbol{\phi}$	Eigenvector
Ψ	Response function

CONTENTS

1

INTRODUCTION

Structural designing is a complex human process that requires comprehensive understanding of the problem and creativity. For centuries, these physical problems have been examined by making mathematical models, and since the availability of computers, it was also tried to automate the creative part by using smart mathematical optimization algorithms. However, as the problems and models become increasingly complex, also the design task gets more difficult. In the present work it is tried to bridge the gap between geometrically nonlinear structures and topology optimization.

1.1 TOPOLOGY OPTIMIZATION

The purpose of topology optimization is to find the optimal layout of a structure within a specified region. It involves the determination of features such as holes and the connectivity of the domain. The goal is for example to maximize the stiffness of a structure for a given amount of material, or to design compliant mechanisms that transfer forces or displacements through elastic deformation.

Often such structures show poor performance or even fail when they are subjected to realistic loads [1]. For example, slender struts, which are a typical result of topology optimization, tend to buckle before the structure is completely loaded. These effects are not taken into account when the optimization is based on a linear model. When external loads applied to the structure become large, the displacements and rotations may also become large. In this case we say that the structure is geometrically nonlinear. In contrast to topology optimization of linear structural problems, much less attention has been paid to topology optimization of geometrically nonlinear structural problems.

The objective of this work is to implement a method to solve topology optimization problems under large displacements and rotations. The main focus is on designing stiff structures, but also an outlook on designing structures that follow a prescribed equilibrium path is presented.

1.2 APPLICATIONS

There are many applications in which topology optimization of geometrically nonlinear structures can be useful. For example, a conventional plaster cast can be replaced by a plastic shell structure, as in Figure 1.1a. The cast is required to be very stiff, but at the same time it desired to be lightweight to be more patient friendly. When such a cast is designed using topology optimization based on linear analysis, the cast might look very stiff. However, in reality it may buckle due to nonlinear effects that have not been taken into account. In the present work we investigate the differences in designs based on linear and nonlinear analysis. Another application one can think of are rubber seals, see Figure 1.1c. Although these seals can undergo finite displacements and rotations, they are required to be stiff in some directions.

Topology optimization is also very suitable for designing compliant mechanisms. In many cases compliant mechanisms undergo finite displacements and rotations and, therefore, taking into account geometrical nonlinearities is essential. For example, if a disabled person has difficulties lifting his arm, a body support structure could be designed that follows the right load-deflection curve (or equilibrium path) which helps this person lift his arm. A shell structure, such as in Figure 1.1b, could be particularly suitable for this task since it can exhibit high nonlinear behavior and can be worn close to the body.

Other very promising applications lie in the field of MicroElectroMechanical Systems (MEMS). If the equilibrium path of a structure can be prescribed by the designer, it can also contain multiple stable equilibrium states. An example of this is the bistable MEMS mechanism in Figure 1.1d that is used as an optical switch. It exhibits snap-through behavior and is therefore well-suited for rapid switching operations. It can be held in both stable configurations without the need for an external force.

Structures exhibiting geometric hardening or softening behavior can also be utilized for crash worthiness or energy absorption. For example, one may wish to find a structure which can absorb a specific amount of energy in case of impact. Structures designed using topology optimization often have complex shapes. Thanks to the development of additive manufacturing techniques (3D printing), these structures are nowadays relatively easy to produce [2].

1.3 PROBLEM STATEMENT

The aim of the present work is to develop and implement the numerical tools required for topology optimization of geometrically nonlinear structures. It is divided into three main goals:

1. Implement the Newton-Raphson incremental-iterative procedure in combination with arc-length control to carry out the nonlinear analysis.
2. Investigate whether load dependent Ritz vectors can be used to create a reduced-order model, to decrease the computational costs of the nonlinear analyses.
3. Implement the end-compliance minimization problem for the design of stiff geometrically nonlinear structures.

All techniques are implemented in the Python based finite element package hybrida, which is being developed at the department of Precision and Microsystems Engineering of TU Delft. Although it is not the goal to apply this method on the design of a specific structure, several numerical experiments will be conducted to demonstrate the effectiveness of the method. The results will be compared with structures that are obtained using topology optimization based on linear analysis. Particular focus is on shell structures, because they can exhibit very high nonlinear behavior.

1.4 OUTLINE

In Chapter 2 an introduction to nonlinear mechanics will be given. Chapter 3 discusses nonlinear finite element analysis and deals with goal 1 described in the problem statement. Subsequently, in Chapter 4 an overview of reduction methods is given, and it is investigated whether load dependent Ritz vectors can be used to create a reduced-order model, to address goal 2. Chapter 5 is focusing on topology optimization, in particular, end-compliance minimization and deals with goal 3. Chapter 6 provides an outlook for designing structures that follow a prescribed equilibrium path. Finally, conclusions are drawn and recommendations are given in Chapter 7. In Appendix A the stiffness matrices are derived of the elements used in this work.

(a) A cast is a shell structure that is supposed to be very stiff and lightweight the same time. [3]

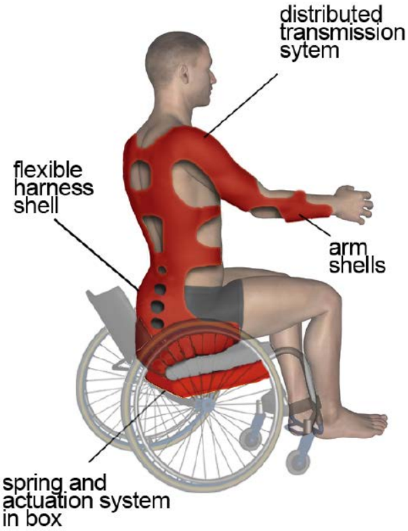

(b) Example of a body support structure that helps a disabled person lift his arm. [3]

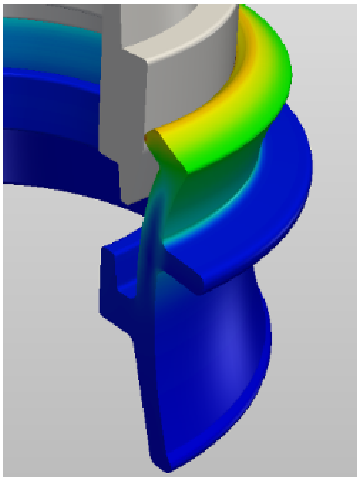

(c) Although rubber seals can undergo finite displacements and rotations, they are required to be stiff in some directions. [4]

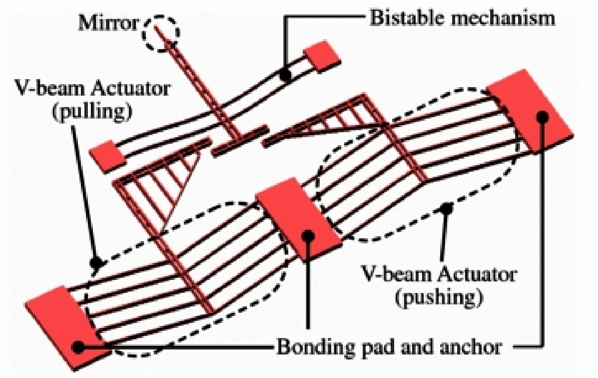

(d) Bistable MEMS mechanism that is used as an optical switch. [5]

Figure 1.1: Several applications for topology optimization of geometrically nonlinear structures.

2

INTRODUCTION TO NONLINEAR MECHANICS

In this chapter some of the fundamentals of nonlinear mechanics are presented. It is assumed that the problem is already discretized using the finite element method and that the system is conservative, which means the total energy is constant. The focus is on structures that undergo finite displacements and rotations, i.e: geometrically nonlinear problems.

2.1 NONLINEAR MECHANICS

Structural mechanics is based on three main ingredients: continuity, equilibrium and a constitutive relation. The continuity equation relates the variation of displacements to the variation of strains or deformations by means of the strain-displacement matrix **B** which is a function of the displacements. **B** contains the derivatives of the shape functions:

$$\delta\boldsymbol{\varepsilon} = \mathbf{B}(\mathbf{u})\delta\mathbf{u}, \qquad B_{ij} = \frac{\partial \varepsilon_i}{\partial u_j}. \tag{2.1}$$

The principle of virtual work is employed to derive the static equilibrium equation. The internal virtual work on element level is defined as

$$\delta W_{\text{int}} = \int_{V_e} \boldsymbol{\sigma}^\top \delta\boldsymbol{\varepsilon}\, \mathrm{d}V_e, \tag{2.2}$$

where $\boldsymbol{\sigma}$ is the second Piola-Kirchhoff stress vector and $\boldsymbol{\varepsilon}$ the Green-Lagrange deformation vector. They are energetically conjugated, which means their inner product has the unit of work. The external virtual work is defined as the inner product of the external force **f** and the virtual displacements $\delta\mathbf{u}$:

$$\delta W_{\text{ext}} = \mathbf{f}^\top \delta\mathbf{u}. \tag{2.3}$$

The equilibrium condition states that the internal virtual work needs to be equal to the external virtual work. When the variation of deformation in Equation 2.1 is substituted in Equation 2.2, this leads to

$$\int_{V_e} \boldsymbol{\sigma}^\top \mathbf{B}\,\delta\mathbf{u}\,\mathrm{d}V_e = \mathbf{f}^\top \delta\mathbf{u}. \tag{2.4}$$

This expression has to hold for every virtual displacement $\delta\mathbf{u}$. After taking the transpose of both sides, this results in

$$\mathbf{f} = \int_{V_e} \mathbf{B}^\top \boldsymbol{\sigma}\,\mathrm{d}V_e. \tag{2.5}$$

Finally, a constitutive relation can be used to find an expression for the stresses. A linear elastic material model is used, so this expression can be formulated as

$$\boldsymbol{\sigma} = \mathbf{D}\boldsymbol{\varepsilon}. \tag{2.6}$$

Here $\mathbf{D}$ is the constitutive matrix. We consider finite displacements and rotations, but small deformations and no material nonlinearities. Therefore the stresses are related to the deformations linearly, which means $\mathbf{D}$ is *not* a function of $\mathbf{u}$.

2.2 RATE EQUATIONS

Because the problem is nonlinear, load and displacement are not linearly related. Therefore, we rather look at the linear relation between increments of the load and increments of the displacement. This is described by the so-called rate equation. The rate equation is obtained by differentiating Equation 2.5 with respect to pseudo-time. In pseudo-time inertia effects are not taken into account, but it tells how the load is applied in steps:

$$\dot{\mathbf{f}} = \int_{V_e} \left(\mathbf{B}^\top \dot{\boldsymbol{\sigma}} + \dot{\mathbf{B}}^\top \boldsymbol{\sigma} \right) \mathrm{d}V_e. \tag{2.7}$$

The stress rate $\dot{\boldsymbol{\sigma}}$ is obtained by differentiating the constitutive relation in Equation 2.6 with respect to time. We recall that the constitutive matrix $\mathbf{D}$ is constant, which means its derivative with respect to time is zero:

$$\dot{\boldsymbol{\sigma}} = \mathbf{D}\dot{\boldsymbol{\varepsilon}} = \mathbf{D}\mathbf{B}\dot{\mathbf{u}}. \tag{2.8}$$

The rate of the strain-displacement matrix $\dot{\mathbf{B}}$ is obtained by applying the chain rule:

$$\dot{\mathbf{B}} = \frac{\mathrm{d}}{\mathrm{d}t}\left(\frac{\partial \varepsilon_k}{\partial u_j} \right) = \frac{\partial^2 \varepsilon_k}{\partial u_i \partial u_j} \frac{\mathrm{d}u_i}{\mathrm{d}t}. \tag{2.9}$$

Substituting Equations 2.8 and 2.9 in Equation 2.7 and using index notation gives

$$\dot{f}_i = \int_{V_e} \left(B_{ki} D_{kl} B_{lj} + \frac{\partial^2 \varepsilon_k}{\partial u_i \partial u_j} \sigma_k \right) \mathrm{d}V_e \, \dot{u}_j, \tag{2.10}$$

or using matrix notation

$$\dot{\mathbf{f}} = \int_{V_e} \left(\mathbf{B}^\top \mathbf{D}\mathbf{B} + \mathbf{G}^\top \mathbf{S}\mathbf{G} \right) \mathrm{d}V_e \, \dot{\mathbf{u}}, \tag{2.11}$$

where the matrix $\mathbf{S}$ contains the second Piola-Kirchhoff stress components and the matrix $\mathbf{G}$ contains, just like $\mathbf{B}$, the spatial derivatives of the shape functions, but in a different order.

The first term in the brackets is referred to as the material or physical stiffness matrix $\mathbf{K}_\mathrm{M}$. It takes into account the stiffness of the material and is similar to the stiffness matrix in linear problems. However, in this case the material stiffness can be a function of the displacement, because $\mathbf{B}$ is a function of the displacement. The second term in the brackets is referred to as the geometric stiffness matrix $\mathbf{K}_\mathrm{G}$. It takes into account that the stresses might have an effect on the stiffness. The geometric stiffness is also a function of the displacement. The material and geometric stiffness matrix can be expressed in both index and matrix notation:

$$K^e_{\mathrm{M}_{ij}} = \int_{V_e} B_{ki} D_{kl} B_{lj} \, \mathrm{d}V_e \qquad \mathbf{K}^e_\mathrm{M} = \int_{V_e} \mathbf{B}^\top \mathbf{D}\mathbf{B} \, \mathrm{d}V_e, \tag{2.12}$$

$$K^e_{\mathrm{G}_{ij}} = \int_{V_e} \frac{\partial^2 \varepsilon_k}{\partial u_i \partial u_j} \sigma_k \, \mathrm{d}V_e \qquad \mathbf{K}^e_\mathrm{G} = \int_{V_e} \mathbf{G}^\top \mathbf{S}\mathbf{G} \, \mathrm{d}V_e. \tag{2.13}$$

Note that the structure of these matrices depends on the element type. After assembling, the sum of the material and geometric stiffness matrix is tangent stiffness matrix. It represents the current stiffness of the structure:

$$\mathbf{K} = \mathbf{K}_{\mathrm{M}} + \mathbf{K}_{\mathrm{G}}. \tag{2.14}$$

The rate in Equation 2.11 comes down to

$$\left(\mathbf{K}_{\mathrm{M}} + \mathbf{K}_{\mathrm{G}}\right)\dot{\mathbf{u}} = \dot{\mathbf{f}}, \tag{2.15}$$

or

$$\mathbf{K}\dot{\mathbf{u}} = \dot{\mathbf{f}}, \tag{2.16}$$

when the tangent stiffness matrix is used.

2.3 STABILITY POINTS

The (external) force $\mathbf{f}$ can be written as the product of a normalized constant spatial distribution $\hat{\mathbf{f}}$ and a load parameter λ. This allows to scale the load using the load parameter λ:

$$\mathbf{f} = \lambda\,\hat{\mathbf{f}}. \tag{2.17}$$

The nonlinear finite element problem is described as

$$\mathbf{K}\dot{\mathbf{u}} = \dot{\lambda}\,\hat{\mathbf{f}}. \tag{2.18}$$

To be able to solve this equation, $\mathbf{K}$ needs to be regular, which means it can be inverted and has therefore no zero eigenvalue. If this is not the case, we are dealing with a stability point which complicates the computations. There are two types of stability points, as will be shown now.

Let $\mathbf{w}$ be an eigenvector of $\mathbf{K}$ corresponding to a zero eigenvalue, i.e:

$$\mathbf{K}\mathbf{w} = \mathbf{0}, \quad \mathbf{w} \neq \mathbf{0}. \tag{2.19}$$

Pre-multiplying the rate Equation 2.18 by $\mathbf{w}$ yields

$$\mathbf{w}^{\top}\mathbf{K}\dot{\mathbf{u}} = \dot{\lambda}\,\mathbf{w}^{\top}\hat{\mathbf{f}}. \tag{2.20}$$

Making use of Equation 2.19 and the fact that $\mathbf{K}$ is symmetric gives $\mathbf{w}^{\top}\mathbf{K} = \mathbf{0}^{\top}$. Therefore, Equation 2.20 comes down to

$$\dot{\lambda}\,\mathbf{w}^{\top}\hat{\mathbf{f}} = \mathbf{0}. \tag{2.21}$$

This results in two possibilities:

1. $\dot{\lambda} = 0$: which means the load is constant, as illustrated in Figure 2.1a. This is called a limit point in the load. In Chapter 3 a method is presented to overcome such a limit point.

2. $\mathbf{w}^{\top}\hat{\mathbf{f}} = 0$: which means the velocity field is orthogonal to the load, which means there is a second solution we can escape to, see Figure 2.1b. This is called a bifurcation point and will be discussed in Section 2.3.1.

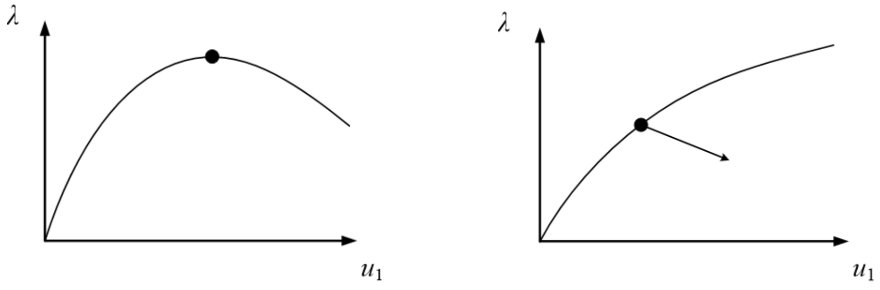

(a) Load limit point. (b) Bifurcation point.

Figure 2.1: A limit point in the load and a bifurcation point are both stability points. At these points the tangent stiffness matrix is singular.

2.3.1 LINEAR PREBUCKLING ANALYSIS

Buckling or bifurcation occurs when a structure reaches a bifurcation point. This is a point where two or more equilibrium paths intersect. The equilibrium paths and the bifurcation points can be found by carrying out a full nonlinear analysis. This can be done using a path-following technique such as the arc-length control method. The biggest advantage of this full nonlinear analysis is that the complete postbuckling behavior can be evaluated. Moreover, little assumptions are made about the structure and the procedure works for any structure with any imperfections. However, a full nonlinear analysis is computationally expensive. Especially when it is used in topology optimization, when many function evaluations are needed.

An alternative option is to analyze the structure using linear prebuckling analysis. After making several assumptions, this method leads to a linear eigenvalue problem. The main drawbacks of linear prebuckling analysis is that it can only provide information on bifurcation points located on an undeflected primary path. Therefore, all information on postbuckling behavior is lost [6].

It is assumed that the system is conservative and that the tangent stiffness matrix is decomposed into the material en geometric stiffness matrix as in Equation 2.14. The material stiffness matrix is the same as in linear problems, because it is evaluated in the undeformed configuration, so $\mathbf{K}_\mathrm{M}$ stays constant during loading. It is also assumed that $\mathbf{K}_\mathrm{G}$ is zero in the undeformed configuration and that is scales linearly with λ during loading. The structure loses its stability when the tangent stiffness matrix becomes singular, that is

$$(\mathbf{K}_\mathrm{M} + \lambda\,\mathbf{K}_\mathrm{G})\,\mathbf{w} = \mathbf{0}, \tag{2.22}$$

for a mode shape $\mathbf{w} \neq \mathbf{0}$. The eigenvalues λ_i are the buckling loads (or critical loads), which are the loads at which the structure starts to buckle. The eigenvectors $\mathbf{w}_i$ are the corresponding buckling modes, which are the directions in which the structure starts to buckle. The normalized buckling modes are orthogonal to the load vector:

$$\mathbf{w}^\top \hat{\mathbf{f}} = 0. \tag{2.23}$$

As pointed out before, the most important assumption made in linear prebuckling analysis is that the load $\mathbf{f}$, displacement $\mathbf{u}$, stresses $\boldsymbol{\sigma}$ and the geometric stiffness matrix $\mathbf{K}_\mathrm{G}$ scale linearly with the load parameter λ. This assumption holds when the structure does not undergo finite displacements or rotations before the buckling load is reached.

2.4 ELEMENT DESCRIPTION

This section gives a short description of the elements used in the present work.

TRUSS ELEMENT

The nonlinear 2D truss element is implemented based on a Total Lagrange formulation. The material and geometric stiffness matrices are derived in Appendix A.1.

SHELL ELEMENT

The shell element used in this work is a finite rotation Kirchhoff shell element implemented by Smit [7]. It is constructed by a combination of a constant strain triangle and a constant moment plate bending element formulated by an assumed stress hybrid formulation. For the membrane part of the element a Total Lagrange formulation is used and for the bending part a corotation formulation is used. For most problems in this work an inconsistent tangent stiffness matrix is used to speed up the computations. This implies that the bending contributions in the geometric stiffness matrix are neglected. The derivation of the material and geometric stiffness matrix of this nonlinear 3D triangular membrane element is given in Appendix A.2. Solely in the convergence plot in Figure 3.13 the consistent tangent is used, to show the quadratic convergence behavior of the Newton-Raphson procedure. For a more extensive derivation of the element, the reader is referred to [8] and [9].

CONTINUUM ELEMENT

The 2D continuum triangular element is similar to the shell element, with the only difference that the out-of-plane displacements and rotations are constrained. Therefore, it uses the consistent tangent stiffness matrix that is derived in Appendix A.2

3

NONLINEAR FINITE ELEMENT ANALYSIS

In this chapter a method is presented to solve the nonlinear finite element problem described in Chapter 2. Depending on the problem and the severity of the nonlinearities, different solution schemes are required to trace the entire equilibrium path. A Newton-Raphson scheme is derived independent of the control strategy. This "unified approach" is very powerful and leads to an effective object-oriented implementation.

3.1 NONLINEAR SOLUTION PROCEDURE

In section 2.2 the rate equations of the finite element problem were derived. The concept of pseudo-time can be employed to apply the external load in a number of steps (or increments). Since geometrically nonlinear problems are path-independent, it would in principle be possible to impose the entire external load in a single step. But normally, this is not a sensible approach, because iterations are required to find the solution. For very large loading steps it is usually difficult to obtain a properly converged solution. Furthermore, one is often interested in the full equilibrium path. Therefore, an incremental-iterative solution procedure is best suited for these nonlinear problems [10].

In an incremental-iterative procedure, each load step consists of an increment of the external load and subsequent iterations to restore equilibrium. The most commonly used technique is the Newton-Raphson method, which involves repeated linearization of the nonlinear equations. This technique is very suitable because of its quadratic convergence and because the factorized tangent stiffness matrices can be used later in the sensitivity analysis [11]. The Newton-Raphson incremental-iterative solution procedure is graphically displayed in Figure 3.1a. When no iterations are done, the solution tends to drift away from the true equilibrium path. This procedure is called a purely incremental solution procedure and is shown in Figure 3.1b.

3.2 NONLINEAR ANALYSIS

In Section 3.1 it was assumed, without further remark, that load control is used to control the Newton-Raphson process. However, load control might not be the best control strategy to solve the nonlinear system. In what follows, a more general formulation is derived to control the Newton-Raphson process.

The residual force is defined as the difference between the external and internal force:

$$\mathbf{r} = \mathbf{f}_{\text{ext}} - \mathbf{f}_{\text{int}}. \tag{3.1}$$

The system is in equilibrium if the residual force is equal to zero, so the goal of this procedure is to solve the residual equations

$$\mathbf{r}(\mathbf{u}, \lambda) = \mathbf{0}, \tag{3.2}$$

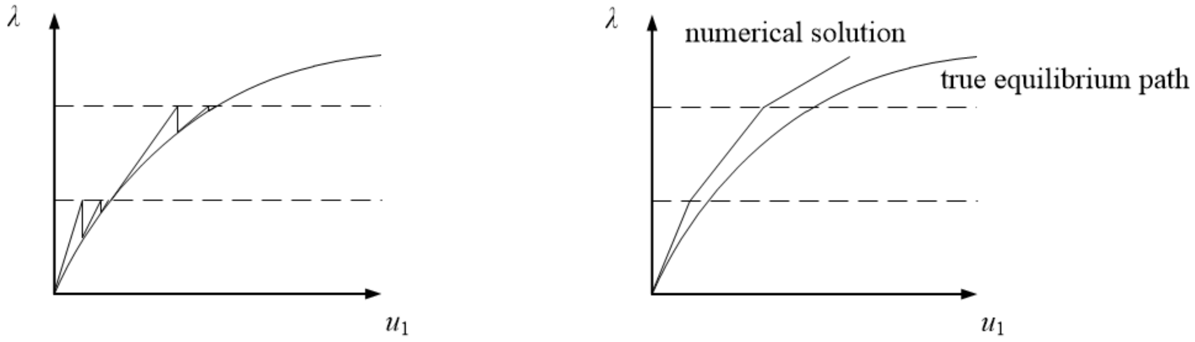

(a) Incremental-iterative solution procedure.

(b) Purely incremental solution procedure.

Figure 3.1: Graphical explanation of the incremental-iterative and the purely incremental solution procedure for one degree of freedom. The purely incremental solution tends to drift away from the true equilibrium path, even when the load increments are very small. In the incremental-iterative solution procedure this is prevented by adding equilibrium iterations within each loading step.

or

$$\mathbf{K}\Delta\mathbf{u} = \mathbf{r}, \tag{3.3}$$

where $\mathbf{r}$ is a function of the displacement $\mathbf{u}$ and the load parameter λ. A load step is imposed by changing the load parameter. Therefore, an additional constraint equation is needed. The constraint equations enables the use of several control strategies, such as: load control, displacement control and arc-length control, as will be discussed later. These control strategies have different constraint equations, but they can all be casted in the same form:

$$c(\mathbf{u}, \lambda) = 0. \tag{3.4}$$

This general formulation of the control strategy, called the unified approach, is implemented in hybrida, which enables very easy switching between different control strategy classes. Moreover, new control strategies can be added by adding only a few lines of code, without the need of writing a completely new Newton-Raphson procedure. This is remarkable because the control strategies are physically very different.

Starting from $\lambda = 0$, we want to calculate a series of solutions $\mathbf{u}$ and corresponding λ's. We define the last accepted solution at time t as $\mathbf{u}^t$, λ^t, and the next target solution at time $t+\Delta t$ as $\mathbf{u}^{t+\Delta t}$, $\lambda^{t+\Delta t}$. The next target solution has to satisfy, within a specified tolerance, the nonlinear system of equations:

$$\mathbf{r}(\mathbf{u}^{t+\Delta t}, \lambda^{t+\Delta t}) = \mathbf{0}, \qquad c(\Delta\mathbf{u}^t, \Delta\lambda^t) = 0, \tag{3.5}$$

in which

$$\Delta\mathbf{u}^t = \mathbf{u}^{t+\Delta t} - \mathbf{u}^t, \qquad \Delta\lambda^t = \lambda^{t+\Delta t} - \lambda^t, \tag{3.6}$$

are the incremental displacement and the incremental load parameter. From now on we assume there is equilibrium at time t and we look for the solution at time $t+\Delta t$. For reasons of readability these superscripts will be omitted. The Newton-Raphson process is applied to the algebraic system in Equation 3.5 to generate a sequence of iterates:

$$\mathbf{u}_j, \qquad \lambda_j, \tag{3.7}$$

in which $j = 1, 2, \ldots$ is the iteration index.

In the Newton-Raphson process, the algebraic system in Equation 3.5 is linearized about the last iterate $(\mathbf{u}_j, \lambda_j)$ using a first order Taylor series expansion:

$$\begin{aligned} \mathbf{r}_{j+1} &= \mathbf{r}_j + \frac{\partial \mathbf{r}}{\partial \mathbf{u}}(\mathbf{u}_{j+1} - \mathbf{u}_j) + \frac{\partial \mathbf{r}}{\partial \lambda}(\lambda_{j+1} - \lambda_j), \\ c_{j+1} &= c_j + \frac{\partial c}{\partial \mathbf{u}}(\mathbf{u}_{j+1} - \mathbf{u}_j) + \frac{\partial c}{\partial \lambda}(\lambda_{j+1} - \lambda_j). \end{aligned} \tag{3.8}$$

In this linearized system the partial derivatives can be expressed as follows:

$$\mathbf{K} = -\frac{\partial \mathbf{r}}{\partial \mathbf{u}}, \quad \hat{\mathbf{f}}_{\text{ext}} = \frac{\partial \mathbf{r}}{\partial \lambda}, \quad \mathbf{a}^\top = \frac{\partial c}{\partial \mathbf{u}}, \quad g = \frac{\partial c}{\partial \lambda}. \tag{3.9}$$

The iterative displacements and the iterative load are defined as follows:

$$\delta \mathbf{u}_{j+1} = \Delta \mathbf{u}_{j+1} - \Delta \mathbf{u}_j, \qquad \delta \lambda_{j+1} = \Delta \lambda_{j+1} - \Delta \lambda_j. \tag{3.10}$$

In this section the δ-operator represents an iteration difference and not a variation. This notation is used to distinguish the increments in Equation 3.6 from the iterations in Equation 3.10. The linearized system in Equation 3.8 can now be casted in matrix form:

$$\begin{bmatrix} \mathbf{K} & -\hat{\mathbf{f}}_{\text{ext}} \\ \mathbf{a}^\top & g \end{bmatrix} \begin{bmatrix} \delta \mathbf{u}_{j+1} \\ \delta \lambda_{j+1} \end{bmatrix} = \begin{bmatrix} \mathbf{r}_j \\ -c_{j+1} \end{bmatrix}. \tag{3.11}$$

Equation 3.11 is an augmented version of Equation 3.3. The iterative load parameter was added as an extra unknown, and, to be able to solve the system, a constraint equation was added.

A big disadvantage of the augmented system in Equation 3.11 is that the symmetry and banded structure of the (augmented) stiffness matrix is destroyed. Solving this system with a traditional method would be computationally undesirable with respect to both storage and efficiency. However, Batoz and Dhatt [12] presented a technique to overcome this problem. The iterative displacement vector can be split into two components, which leads to an uncoupled system of equations:

$$\delta \mathbf{u}_{j+1} = \delta \mathbf{u}_{j+1}^{\text{res}} + \delta \lambda_{j+1} \delta \mathbf{u}_{j+1}^{\text{ext}}. \tag{3.12}$$

The first component $\delta \mathbf{u}_{j+1}^{\text{res}}$ is the displacement as a result of the residual force and the second component $\delta \mathbf{u}_{j+1}^{\text{ext}}$ is the displacement purely caused by the external unit force. They are computed by solving the following two systems of equations:

$$\mathbf{K} \delta \mathbf{u}_{j+1}^{\text{res}} = \mathbf{r}_j, \qquad \mathbf{K} \delta \mathbf{u}_{j+1}^{\text{ext}} = \hat{\mathbf{f}}_{\text{ext}}. \tag{3.13}$$

Note that the stiffness matrix only has to be inverted once (using LU factorization [13]), and that the symmetric and banded properties are retained. The only thing left to compute is the iterative load parameter $\delta \lambda_{j+1}$. This value depends on the constraint equation and thus the control strategy.

3.3 INCREMENTAL CONTROL STRATEGIES

As presented in Section 3.2, there exists several constraint equations. Each constraint equation represents a constraint surface, on which we search for the intersection with the equilibrium path. The constraint equations for load control, displacement control and arc-length control are given in Table 3.1.

3.3.1 LOAD CONTROL

Load control is the easiest and most commonly used strategy. An external load $l = \overline{\Delta \lambda}$ is prescribed at the beginning of the load step and held constant throughout the remaining iterations. Hence, the load parameter is

$$\delta \lambda_{j+1} = \begin{cases} \overline{\Delta \lambda} & \text{for} \quad j = 0 \\ 0 & \text{for} \quad j \geq 1. \end{cases} \tag{3.14}$$

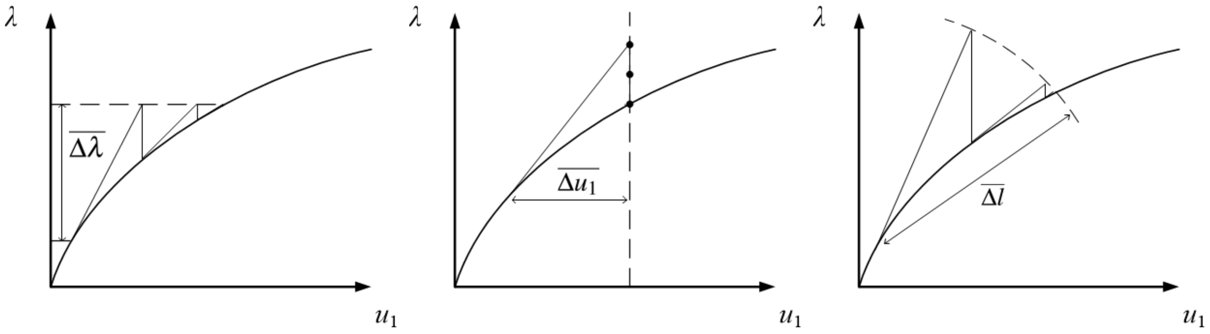

(a) Load control. (b) Displacement control. (c) Arc-length control.

Figure 3.2: Graphical explanation of the most commonly used control strategies.

The constraint surface is a horizontal line in the load-displacement diagram for one degree of freedom, see Figure 3.2a. This strategy is widely used but cannot overcome limit points in the load, because no intersection exists, see Figure 2.1a. Therefore, load control cannot be used for analyzing structures exhibiting snap-through.

3.3.2 DISPLACEMENT CONTROL

Another popular strategy is displacement control. Analogous to load control, displacement control uses a fixed displacement component as the control parameter to trace the equilibrium path. This prescribed displacement for a specified control degree of freedom is called $l = \overline{\Delta u}_{\text{ctrl}}$. From the constraint equation in Table 3.1 it can be derived that the corresponding load parameter is

$$\delta\lambda_{j+1} = \begin{cases} \dfrac{\overline{\Delta u}_{\text{ctrl}}}{\delta u^{\text{ext}}_{\text{ctrl},j+1}} & \text{for} \quad j = 0 \\[2ex] -\dfrac{\delta u^{\text{res}}_{\text{ctrl},j+1}}{\delta u^{\text{ext}}_{\text{ctrl},j+1}} & \text{for} \quad j \geq 1. \end{cases} \tag{3.15}$$

The constraint surface is a vertical line in the load-displacement diagram for one dimension, see Figure 3.2b. Therefore, displacement control can overcome limit points in the load, but not in the displacement. Hence, displacement control cannot be used for analyzing structures exhibiting snap-back.

3.3.3 ARC-LENGTH CONTROL

One of the most robust control strategies is arc-length control. It considers simultaneously iterations on both the load and displacement variables. The premise of the method is to constrain the equilibrium path to an arc-length Δl, as indicated in Figure 3.2c. Several versions of the arc-length control strategy exist, depending on the value of the scaling parameter β in the constraint equation in Table 3.1. For spherical arc-length control the value of β has to be set equal to one, for cylindrical arc-length control the value of β has to be set equal to zero, and for elliptical arc-length control any value of β can be chosen, as long as $\beta > 0$ and $\beta \neq 1$. The constraint surfaces corresponding to the three versions are respectively a hypersphere, a hypercylinder and a hyperellipsoid, see Figure 3.3.

Literature states that the value of β does not influence the performance very much and that cylindrical arc-length control shows in fact the most robust behaviour [14]. However, numerical experiments in the present work indicate that the value of β does have a large influence. Since loads and displacements usually have very different orders of magnitudes, for example kN versus mm, the load has to be scaled down using a small value for β, which is in this case approximately 10^{-6}. In addition, for very large values of β, arc-length control resembles load control because the constraint surface is almost horizontal, while for very small values of β, arc-length control resembles displacement control because the constraint surface is almost vertical. In the latter case it is more difficult to overcome limit points in the displacement.

The arc-length constraint equation in Table 3.1 is quadratic, which means it is somewhat expensive to compute $\delta\lambda$. Moreover, the quadratic equations has two roots, which are the two intersections of the constraint surface with the equilibrium path. This is an additional difficulty because it is not always straightforward which root to choose, especially when the equilibrium path exhibits sharp turns. For these two reasons the constraint equation is linearized and the iterations are processed on a tangent hyperplane to the constraint surface, see Figure 3.4. The expression for the load parameter in linearized arc-length control is

$$\delta\lambda_{j+1} = \begin{cases} \pm\dfrac{\overline{\Delta l}}{\sqrt{\delta\mathbf{u}_1^{\text{ext}}\cdot\delta\mathbf{u}_1^{\text{ext}}+\beta^2}} & \text{for} \quad j=0 \\ -\dfrac{\delta\mathbf{u}_1\cdot\delta\mathbf{u}_{j+1}^{\text{res}}}{\delta\mathbf{u}_1\cdot\delta\mathbf{u}_{j+1}^{\text{ext}}+\beta^2\delta\lambda_1} & \text{for} \quad j\geq 1, \end{cases} \tag{3.16}$$

where the subscript 1 stands for the first iteration. Arc-length control can overcome limit points in both the load and displacement. In addition, arc-length control tends to converge faster because the constraint surface is perpendicular to the prediction vector.

AUTOMATIC SIGN-SWITCHING

The sign of the load parameter in Equation 3.16 during the first iteration should be positive for loading and negative for unloading. An obvious choice would be to monitor the lowest eigenvalue of the tangent stiffness matrix and to reverse the sign of he load parameter whenever the lowest eigenvalue changes sign. However, it is expensive to compute the eigenvalue and this method gives incorrect results when a bifurcation point is detected. A more heuristic approach is to adopt a sign-switching strategy similar to the one used by Chrisfield [15]:

$$\delta\lambda_{j+1}^{t+\Delta t} = \begin{cases} +|\delta\lambda_{j+1}^{t+\Delta t}| & \text{if} \quad (\Delta\mathbf{u}^t)^\top\delta\mathbf{u}_1^{\text{ext}} > 0 \\ -|\delta\lambda_{j+1}^{t+\Delta t}| & \text{if} \quad (\Delta\mathbf{u}^t)^\top\delta\mathbf{u}_1^{\text{ext}} < 0. \end{cases} \tag{3.17}$$

This approach proved to work properly for the examples presented in this work.

AUTOMATIC STEP SIZE SELECTION

The new arc-length is automatically chosen by the algorithm based on the desired number of iterations per increment N^{des} provided by the user. The estimate for the new arc-length is

$$\Delta l^{\,t+\Delta t} = \Delta l^{\,t}\left(\frac{N^{\text{des}}}{N^t}\right)^{\gamma}, \tag{3.18}$$

where N^t is the number of iterations in the previous increment. The amplification parameter γ determines how radically the arc-length changes. Normally, a good value is $\gamma = 0.5$ [15].

For load and displacement control an easier formulation can be derived, without the need for splitting the iterative displacement into two components. However, the strength of the unified approach presented in this chapter, is that it can be implemented at the top level of a finite element package. This means no modifications have to made in the rest of the finite element code. Moreover, the presented formulation works for every control strategy. This means that other control strategies, for example work control or generalized displacement control, can be implemented very easily by only changing the expression for $\delta\lambda$. This expression can be derived by hand from the constraint equation. The general nonlinear finite element solution procedure, independent of the control strategy used, that is implemented in hybrida is given in Algorithm 1. A force norm is used as convergence criterion, because this is the most strict one.

Table 3.1: Incremental control strategies for the Newton-Raphson process.

Control strategy	Constraint equation c	$\mathbf{a}$	g
Load control	$\delta\lambda - l = 0$	$\mathbf{0}$	1
Displacement control	$\delta\mathbf{u}^\top\delta\mathbf{u} - l^2 = 0$	$2\delta\mathbf{u}$	0
Arc-length control	$\delta\mathbf{u}^\top\delta\mathbf{u} + \beta^2\delta\lambda^2 - l^2 = 0$	$2\delta\mathbf{u}$	$2\delta\lambda$

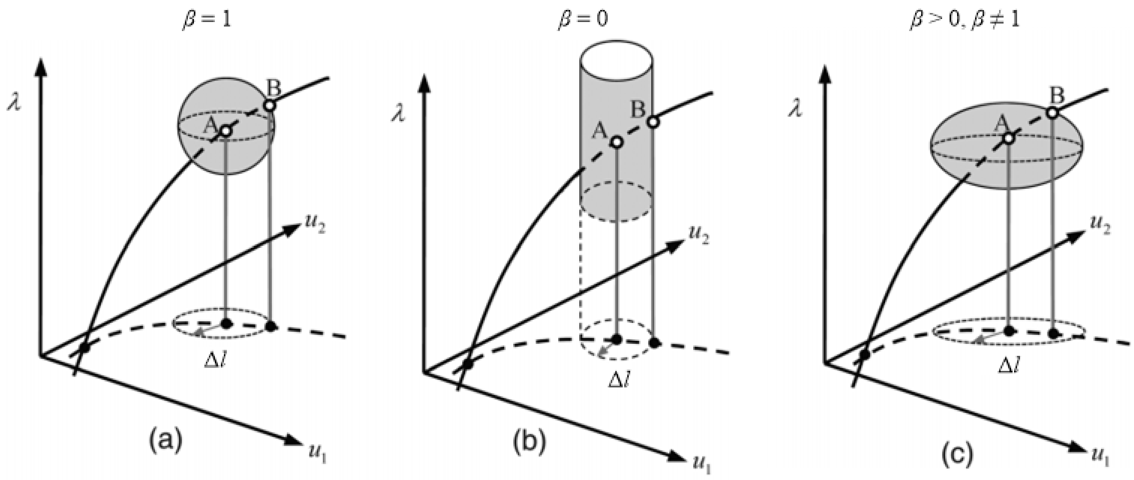

Figure 3.3: (a) spherical, (b) cylindrical and (c) elliptical arc-length control in a two degree of freedom problem. Point A is the last accepted solution at time t and point B is the next target solution at time $t + \Delta t$ [16].

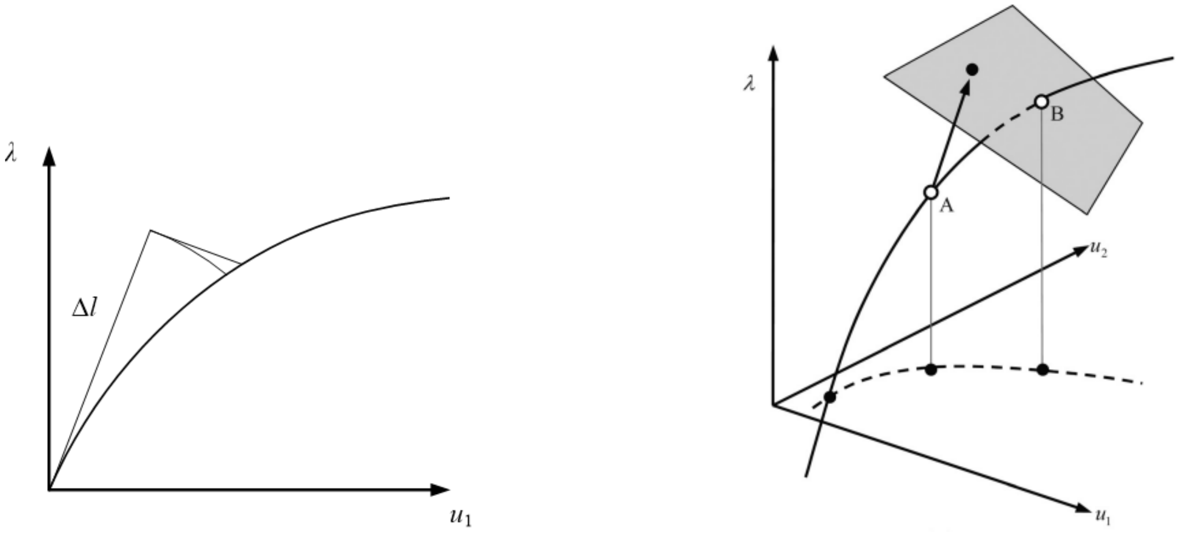

(a) Conventional and linearized arc-length control for one degree of freedom.

(b) Linearized arc-length control for two degrees of freedom.

Figure 3.4: In linearized arc-length control iterations are processed on a tangent hyperplane.

Algorithm 1 Nonlinear finite element solution procedure independent of the control strategy.

```
for each load step do
    Determine new step size $\Delta l$.
    while error > tolerance do
        Set up new tangent stiffness matrix: $\mathbf{K}_e = \int_{V_e} \left( \mathbf{B}^\top \mathbf{D} \mathbf{B} + \mathbf{G}^\top \mathbf{S} \mathbf{G} \right) \mathrm{d}V_e$ and assemble.
        Solve the linear systems $\mathbf{K}\, \delta \mathbf{u}^{\mathrm{res}} = \mathbf{r}$ and $\mathbf{K}\, \delta \mathbf{u}^{\mathrm{ext}} = \hat{\mathbf{f}}_{\mathrm{ext}}$.
        Compute $\delta\lambda$ via one of the constraint equations.
        Add iterative load parameter $\delta\lambda$ to the load parameter: $\lambda = \lambda + \delta\lambda$.
        Compute new external force: $\mathbf{f}_{\mathrm{ext}} = \lambda \hat{\mathbf{f}}_{\mathrm{ext}}$.
        Compute iterative displacement: $\delta \mathbf{u} = \delta \mathbf{u}^{\mathrm{res}} + \delta\lambda\, \delta \mathbf{u}^{\mathrm{ext}}$.
        Add iterative displacement to displacement: $\mathbf{u} = \mathbf{u} + \delta \mathbf{u}$.
        Compute the strain for each integration point $i$: $\boldsymbol{\varepsilon}_i(\mathbf{u})$.
        Compute the stress for each integration point $i$: $\boldsymbol{\sigma}_i = \mathbf{D}\boldsymbol{\varepsilon}_i$.
        Compute new internal force: $\mathbf{f}^{e}_{\mathrm{int}} = \int_{V_e} \mathbf{B}^\top \boldsymbol{\sigma}_i \,\mathrm{d}V_e$ and assemble.
        Compute new residual force: $\mathbf{r} = \mathbf{f}_{\mathrm{ext}} - \mathbf{f}_{\mathrm{int}}$.
        Compute new error: $\dfrac{|\mathbf{r}|}{|\mathbf{r}_1|}$.
```

3.4 NEWTON-RAPHSON SCHEMES

In the full Newton-Raphson scheme the stiffness matrix is set up and decomposed every iteration. This is graphically displayed in Figure 3.5a for one dimension. This leads to the quadratic convergence characteristic of the full Newton-Raphson scheme. However, it is rather costly to compute and decompose the stiffness matrix every iteration. Therefore, variants of the full Newton-Raphson scheme have been developed, to circumvent this decomposition. The three most commonly used variants are discussed here.

The first variant is the modified Newton-Raphson scheme, displayed in Figure 3.5b. In this scheme the stiffness matrix is set up and decomposed only at the beginning of each load step, and is hold constant during the iterations. The drawback is that generally more iterations are required to reach convergence. The modified Newton-Raphson scheme is suitable for problems that do not exhibit very high nonlinearities.

The modified Newton-Raphson scheme can be further simplified by setting up and decomposing the stiffness matrix only at the beginning of the first load step, see Figure 3.5c. It is called the linear elastic scheme, because the stiffness matrix in the undeformed configuration is used during all load steps and iterations. The linear elastic scheme is only suitable for mild nonlinear problems.

The third variant is known under the name quasi-Newton-Raphson scheme, or secant-Newton scheme. In this scheme the stiffness matrix is approximated by a secant approach [10]. A secant stiffness matrix for the next iteration is constructed on the basis of existing knowledge about current values of displacement increments and residual forces calculated within this load step. A secant stiffness can be defined uniquely for one-degree of freedom problems, see Figure 3.5d, but for more-degree of freedom problems there are a lot of possibilities. The quasi-Newton-Raphson scheme does not have a good reputation when it comes to robustness. It sometimes displays an oscillatory type of convergence behaviour and may diverge under certain conditions for reasons that are not clear [14].

The full Newton-Raphson scheme remains most suitable for highly nonlinear problems. Moreover, it is the only scheme that can detect bifurcation points or alternative equilibrium branches that may exist in the system. In addition, when using topology optimization the design of the structure is not known in advance. Therefore, robustness of the analysis is very important and for this reason this scheme will be used in the remainder of this work.

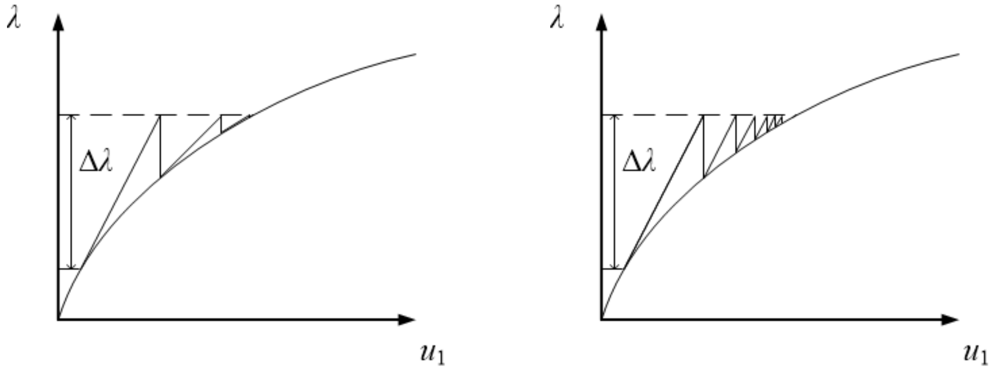

(a) Full Newton-Raphson scheme.

(b) Modified Newton-Raphson scheme.

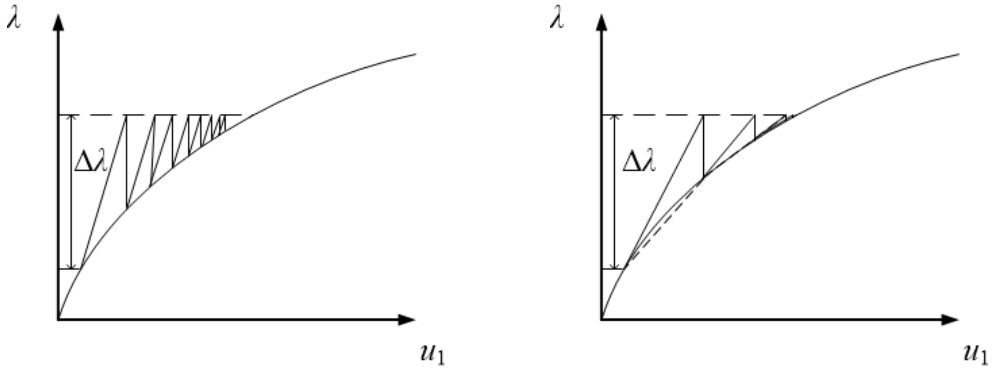

(c) Linear elastic stiffness scheme.

(d) Quasi-Newton-Raphson scheme.

Figure 3.5: Graphical explanation of four different Newton-Raphson schemes for one degree of freedom.

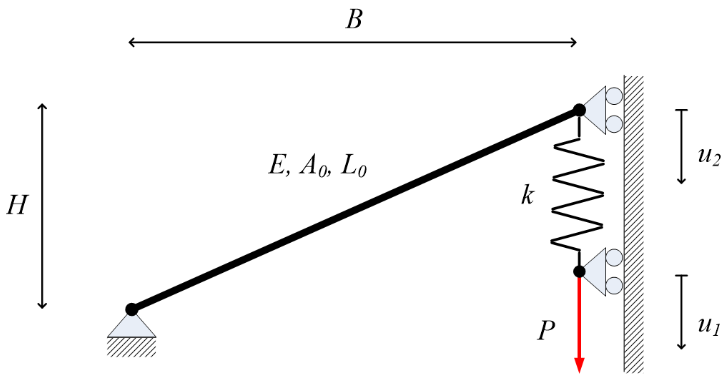

Figure 3.6: Undeformed configuration of the von Mises truss. This simple example has only two degrees of freedom, but can exhibit both snap-through and snap-back behavior. The geometric and material properties are: $B = 1\,\mathrm{m}$, $H = 0.5\,\mathrm{m}$, $L_0 = \sqrt{B^2+H^2} = 1.118\,\mathrm{m}$, $A_0 = 78.5\,\mathrm{mm}^2$ and $E = 70\,\mathrm{GPa}$.

3.5 EXAMPLES USING ARC-LENGTH CONTROL

Two highly nonlinear problems will be analyzed using the Newton-Raphson procedure in combination with arc-length control to demonstrate that the method works.

3.5.1 VON MISES TRUSS

The von Mises truss is a two-degree of freedom system consisting of a (nonlinear) truss element which is indirectly loaded through a spring, as shown in Figure 3.6. Despite its simplicity, the structure can exhibit both snap-through and snap-back behavior, depending on the spring stiffness k. Moreover, an analytical solution can be derived, making it a good example to test the arc-length control strategy in combination with the Newton-Raphson procedure. Large displacements and rotations are accounted for in the Total Lagrangian formulation, with the Green-Lagrange strain as deformation measure.

ANALYTICAL SOLUTION

The analytical solution is derived starting from the potential energy, which consists of a term for the truss, the spring and the load:

$$\Pi = \int_{V_0} \tfrac{1}{2}\sigma\varepsilon \;\mathrm{d}V_0 + \tfrac{1}{2}k(u_1-u_2)^2 - Pu_1. \tag{3.19}$$

Assuming that the stresses and deformations are constant over the truss and recalling that we have to integrate over the undeformed volume, gives $\int_{V_0} \mathrm{d}V_0 = V_0 = A_0L_0$. An expression for the stress is found using Hooke's law, i.e: $\sigma = E\varepsilon$:

$$\Pi = \tfrac{1}{2}EA_0L_0\varepsilon^2 + \tfrac{1}{2}k(u_1-u_2)^2 - Pu_1. \tag{3.20}$$

To satisfy equilibrium, we look for a stationary value of the potential energy. This means that the variation of the potential energy should be zero:

$$\delta\Pi = EA_0L_0\varepsilon\;\delta\varepsilon + k(u_1-u_2)(\delta u_1 - \delta u_2) - P\;\delta u_1 = 0. \tag{3.21}$$

If the deformed length of the truss is

$$L = \sqrt{L_0^2 - 2Hu_2 + u_2^2}, \tag{3.22}$$

then the Green-Lagrange strain can be written as

$$\varepsilon = \frac{L^2 - L_0^2}{2L_0^2} = \frac{u_2^2 - 2Hu_2}{2L_0^2}, \tag{3.23}$$

and the variation of the strain comes down to

$$\delta\varepsilon = \frac{u_2 - H}{L_0^2}\,\delta u_2. \tag{3.24}$$

Substituting this in Equation 3.21 and doing some rearrangements yields

$$\Big(k(u_1-u_2)-P\Big)\;\delta u_1 + \left(EA_0L_0\frac{u_2^2-2Hu_2}{2L_0^2}\frac{u_2-H}{L_0^2}-k(u_1-u_2)\right)\;\delta u_2 = 0. \tag{3.25}$$

This should hold for every value of δu_1 and δu_2, so the two equilibrium equations are

$$\begin{cases} k(u_1-u_2)-P & = 0 \\ EA_0L_0\dfrac{u_2^2-2Hu_2}{2L_0^2}\dfrac{u_2-H}{L_0^2}-k(u_1-u_2) & = 0. \end{cases} \tag{3.26}$$

We are particularly interested in the equilibrium path P versus u_1, but since this curve can contain limit points in both the load and the displacement, it can not be described by a function, e.g: $P(u_1)$ or $u_1(P)$. Instead, the curve can be described by two parametric equations with u_2 as parameter: $P(u_2)$ and $u_1(u_2)$. Adding the two equilibrium equations gives

$$P(u_2) = EA_0L_0\frac{u_2^2-2Hu_2}{2L_0^2}\frac{u_2-H}{L_0^2}, \tag{3.27}$$

and the first equilibrium equation gives

$$u_1(u_2) = \frac{P(u_2)}{k} + u_2. \tag{3.28}$$

It is observed that Equation 3.27 describes the equilibrium path P versus u_2 and that for every value of u_2, the corresponding value of P and u_1 can be found using Equation 3.28.

If the spring stiffness is below a critical value, this results in snap-back behavior in the u_1 component, while values above do not. The critical value is reached when the tangent line to the P versus u_1 curve is vertical, i.e: $\partial P/\partial u_1 \to \infty$ and $u_1 = u_2 = H$ and $P = 0$. The slope of the parametric curve can be calculated using

$$\frac{\partial P}{\partial u_1} = \frac{\left(\dfrac{\partial P}{\partial u_2}\right)}{\left(\dfrac{\partial u_1}{\partial u_2}\right)}. \tag{3.29}$$

Clearly, the slope goes to infinity if $\partial u_1/\partial u_2 = 0$. Solving this for k using Equation 3.28 gives the critical spring stiffness:

$$k_{\mathrm{cr}} = \frac{EAH^2}{2L^3}. \tag{3.30}$$

The behavior of the structure for different values of the spring stiffness is shown in Figure 3.7. The finite element solution is compared to the analytical solution in Figure 3.8. It can be seen that the arc-length control strategy in combination with the Newton-Raphson procedure has no difficulties overcoming the limit points. A constant arc-length was used and a force norm of 10^{-4} as convergence criterion. The formulation of the geometrically nonlinear truss element that was implemented is given in Appendix A.1.

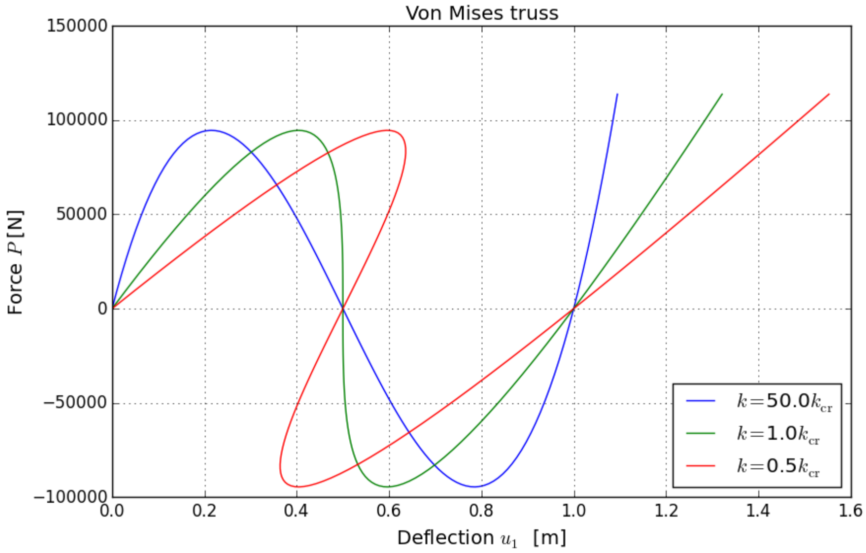

Figure 3.7: Equilibrium path of the von Mises truss for different spring stiffnesses. For the critical spring stiffness the tangent line is vertical at $u_1 = H$. For stiffnesses below the critical value the structure exhibits snap-back behavior. For a stiffness much higher than the critical value the curve resembles the P versus u_2 curve. $k_{\mathrm{cr}} = 491\,488\,\mathrm{N/m}$.

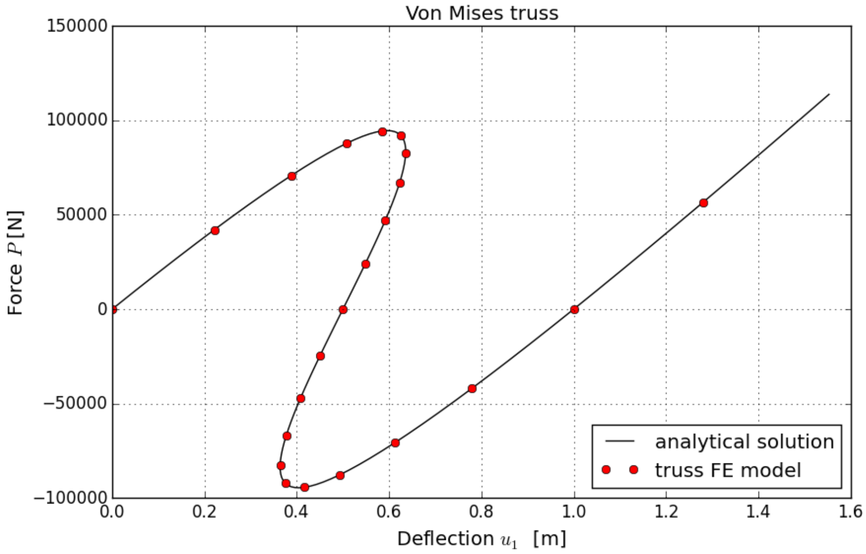

Figure 3.8: The nonlinear finite element solution corresponds to the analytical solution. The spring stiffness is $k = 0.5k_{\mathrm{cr}}$.

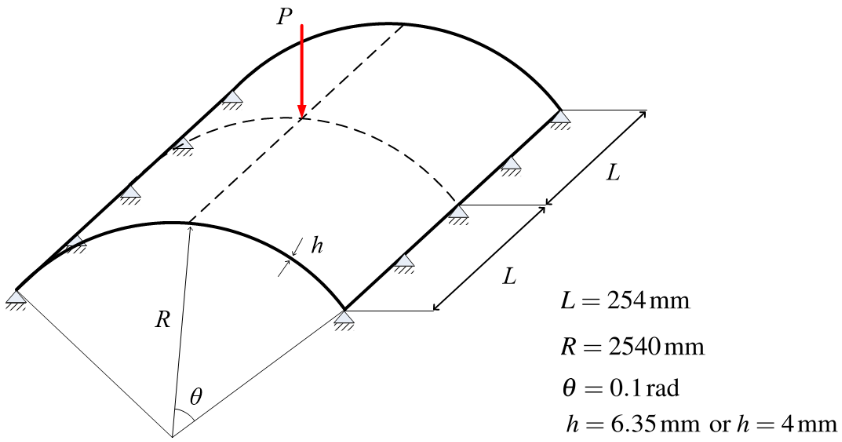

Figure 3.9: Problem of the hinged cylindrical roof. The material properties are: $E = 3.10275\,\mathrm{N/mm^2}$ and $\nu = 0.3$.

3.5.2 Hinged cylindrical roof

To verify the path following capabilities of the nonlinear solution algorithm, the hinged cylindrical roof in Figure 3.9 is analyzed. This problem is chosen because it exhibits dramatic snap-through and snap-back behavior. The roof is double symmetric and is subjected to a concentrated load P in the middle. The rear left quarter is modeled using 88 triangular shell elements and symmetric boundary conditions are applied. The geometric stiffness matrix of this element due to the membrane stresses is derived in Appendix A.2.

The obtained equilibrium path is given in Figure 3.10 for the vertical deflection of the middle of the roof. The thickness is $h = 6.35\,\mathrm{mm}$. Every dot is one increment in the nonlinear analysis. The corresponding number indicates the number of iterations that where required to converge to the equilibrium state. For the tolerance a force norm of 10^{-3} is used. It can be seen that the arc-length control strategy has no difficulties overcoming the limit points and the sharp turns. The automatic step size selection given in Equation 3.18 is used, where the desired number of iterations is 4. Around points (c) and (d) the iterative procedure needs more iterations and the step size is automatically decreased. Towards point (f) the structure behaves close to linear and the step size is increased. The equilibrium path corresponds to the result found in [17]. The displacement fields on the six distinct points (a) to (f) are given in Figure 3.11.

When the thickness of the roof is decreased from $h = 6.35\,\mathrm{mm}$ to $h = 4\,\mathrm{mm}$, the response is completely different, see Figure 3.12. The equilibrium path is a spiral with two stable and two unstable equilibrium states. Again, the arc-length control strategy has no difficulties following the path.
For increment (or time step) 5 the error is plotted in Figure 3.13. The error is defined as the force norm $|\mathbf{r}_j|/|\mathbf{r}_0|$. The plot shows the quadratic convergence behavior which is characteristic for the Newton-Raphson procedure. A consistent tangent is used. In this example the tolerance is set to 10^{-20} to show that the machine accuracy becomes limiting.

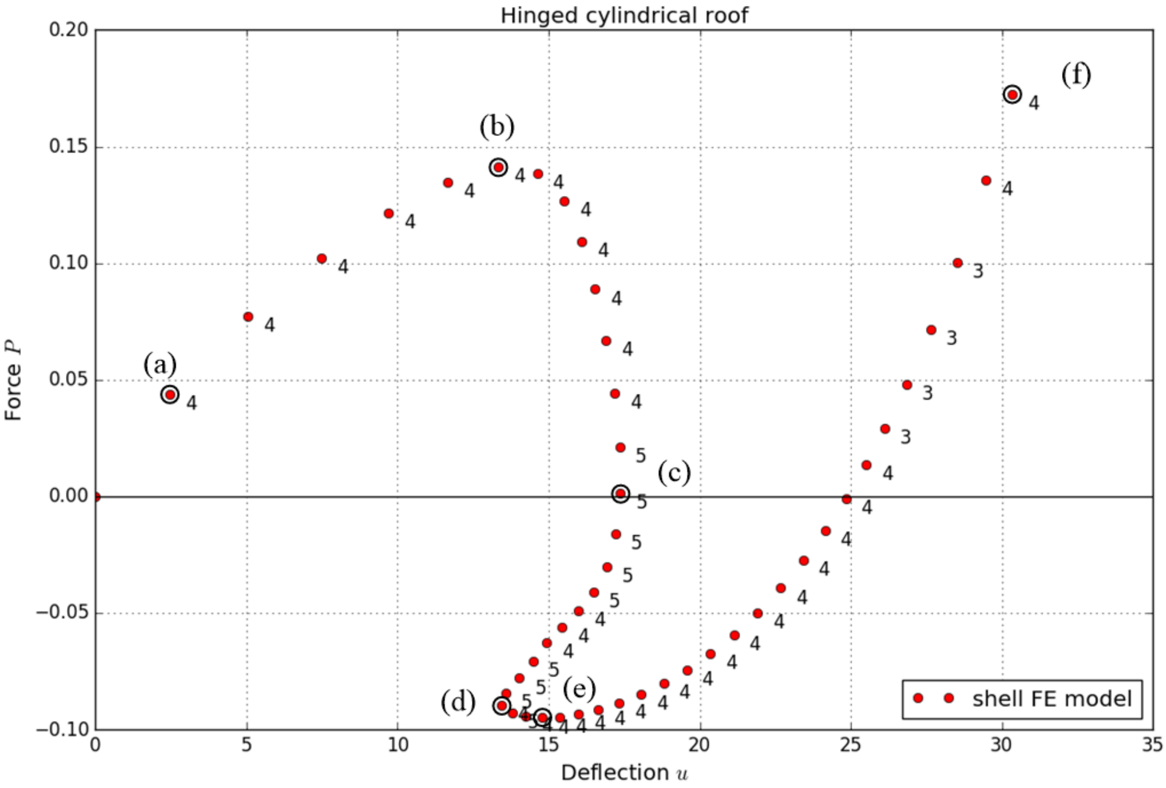

Figure 3.10: Equilibrium path of the hinged cylindrical roof with thickness $h = 6.35\,\mathrm{mm}$. The arc-length control strategy has no difficulties overcoming the limit points.

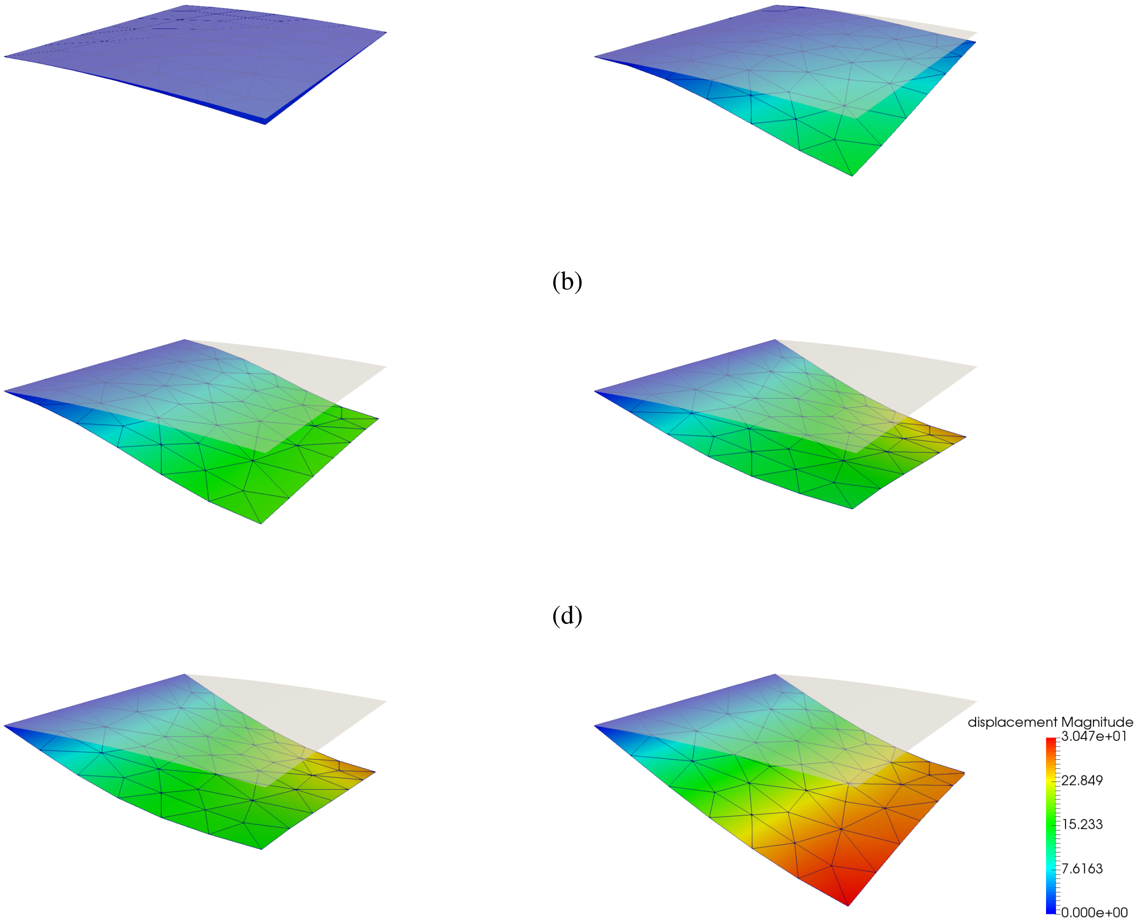

(a) (b) (c) (d) (e) (f)

Figure 3.11: Displacement field of the cylindrical roof at six distinct points indicated in Figure 3.10. The displacement are scaled by a factor of 3.

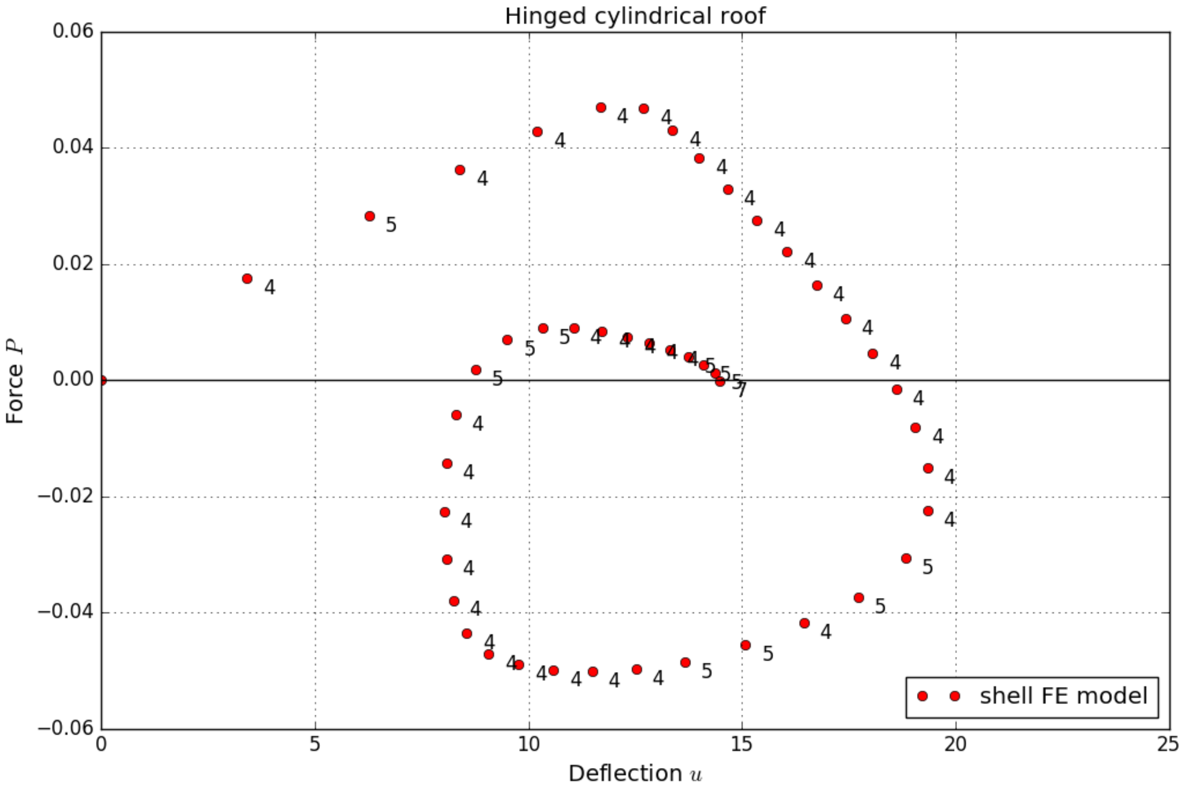

Figure 3.12: Equilibrium path of the hinged cylindrical roof with thickness $h = 4\,\mathrm{mm}$. A slight decrease in thickness gives a totally different response.

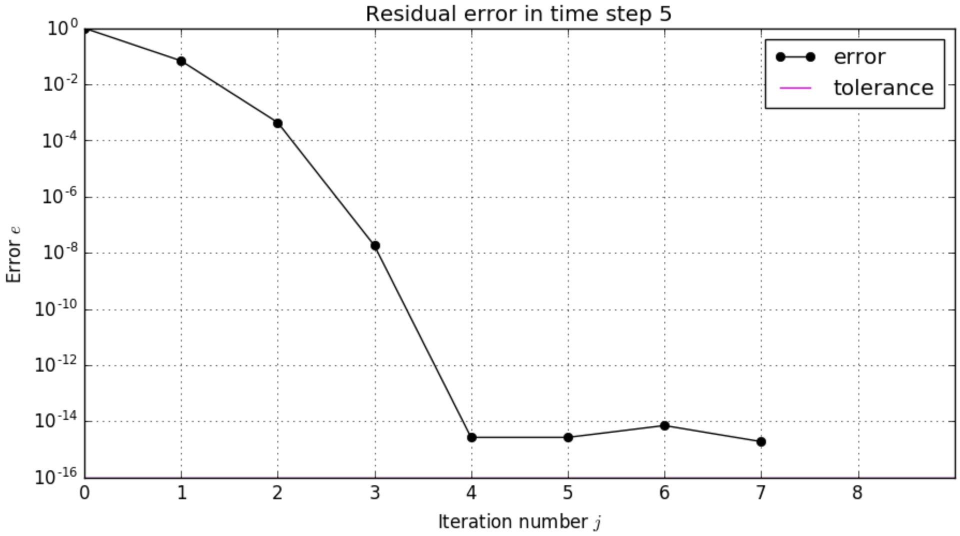

Figure 3.13: Normalized error plot shows the quadratic convergence behavior which is characteristic for the Newton-Raphson procedure. A consistent tangent is used. For a very small tolerance of 10^{-20} the machine accuracy becomes limiting.

4

REDUCTION METHODS

The use of the finite element method to solve nonlinear problems may become very expensive when the number of degrees of freedom becomes very large. Especially when this technique is used in topology optimization, this becomes problematic because a large number of nonlinear problems has to be solved during the design process. Figure 4.1 shows how the nonlinear finite element loop is nested in the optimization loop. A simple example shows us that if a linear finite element analysis takes one minute to solve, and if both the nonlinear finite element analysis and the optimization process need 100 iterations, the computation time is almost a week. This illustrates the desire of reducing the computation time for nonlinear problems.

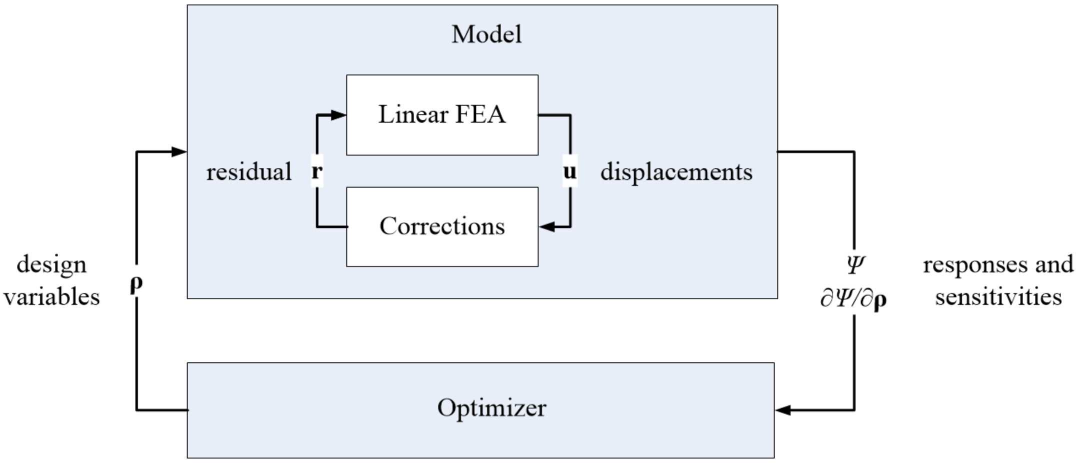

Figure 4.1: The nonlinear finite element analysis loop is nested in the optimization loop, resulting in a large computation time.

4.1 OVERVIEW

Considerable efforts have been made to find ways of reducing the computation time for large-scale nonlinear structural problems. The reduced basis approach aims at savings in computational costs by using a smaller number of generalized variables to represent the original problem [18]. It is assumed that any complicated deformation pattern can be, with sufficient accuracy, represented as a linear combination of a small number of appropriately chosen basis vectors. The effectiveness of this approach depends, to a great extent, on the proper selection of the reduced basis vectors. This section gives an overview of the reduction methods found in literature.

PATH DERIVATIVES

In the eighties Noor *et al.* came up with the use of path derivatives as a reduction method. It uses the displacement vector and its derivatives with respect to the step size control parameter. These vectors are obtained by successive differentiation of the equilibrium equations. Their performance is excellent while dealing with geometrically nonlinear problems. However, it is difficult to extend this approach to account for material nonlinearities. Moreover, the generation of path derivatives is cumbersome; it requires pages of analytical derivations [19]. But the biggest disadvantage is that it is problem dependent [20], [21]. This causes that this method cannot be implemented at the top level of a finite element programme.

PREDICTION AND CORRECTION VECTORS

This method uses the prediction and correction vectors that are computed during the normal course of a nonlinear finite element analysis step [22]. It can be seen as a discrete version of the path derivatives, because the prediction and correction vectors contain information about the nonlinearity. The main advantage of this approach is that no special basis generating procedures are necessary. Also, these basis vectors can be easily computed in the presence of any type of nonlinearity. However, this procedure may fail to converge in the presence of strong nonlinearities [23].

BUCKLING MODE SUPERPOSITION

This method is restricted to cases of mild geometrical nonlinearities which are characterized by the existence of a linear bifurcation situation which is “close” to the considered situation. In this case the true nonlinear behaviour in the initial loading range can be quite well approximated by a linear combination of the eigenvectors (buckling modes) of the linear prebuckling problem. The coefficients corresponding to each buckling mode are nonlinear functions of the load parameter [24].

EIGENVECTORS

For other reduction methods, one might look in the field of linear dynamics, because there, reduction methods are very common. The obvious choice is to use eigenvectors of the tangent stiffness matrix as a reduced basis [1]. The tangent stiffness matrix $\mathbf{K}$ maps a displacement vector $\mathbf{u}$ to a force vector $\mathbf{f}$. If $\mathbf{u}$ and $\mathbf{f}$ point in the same direction, they are called eigenvectors, $\boldsymbol{\phi}$. The ratio of the length of $\mathbf{u}$ and $\mathbf{f}$ is the eigenvalue κ known as the modal stiffness [25]:

$$\mathbf{K}\boldsymbol{\phi} = \kappa\boldsymbol{\phi}. \tag{4.1}$$

The eigenvectors of the tangent stiffness matrix can be understood as the modes of deformation. The first deformation mode is associated with the lowest stiffness.

During the normal course of a nonlinear analysis step using the full Newton-Raphson scheme, truncated sets of eigenvectors of the sequence of updated tangent stiffness matrices are computed. To obtain better results, the eigenvectors can also be supplemented with a few prediction and correction vectors [23]. The results obtained with this method are good. However, it is very expensive to compute eigenvectors. When many eigenvectors are required, this might even become more expensive than factorizing (inverting) the full tangent stiffness matrix repeatedly. Fortunately, the amount of eigenvectors required is limited. Another difficulty is to determine which eigenvectors to choose. Usually the eigenvectors corresponding to the lowest eigenvalues (modal stiffnesses) are chosen, but this might not be the best choice. This means one is still searching for a method that gives a better a representation of the original system, at lower computational costs.

---

[1] The eigenvectors of the tangent stiffness matrix are used, i.e. the matrix $\mathbf{K} = \mathbf{K}_{\mathrm{M}} + \mathbf{K}_{\mathrm{G}}$, while in the buckling mode superposition method the eigenvectors of the matrix $\mathbf{K}_{\mathrm{M}}^{-1}\mathbf{K}_{\mathrm{G}}$ are used.

LOAD DEPENDENT RITZ VECTORS

In the field of linear dynamics another reduction method has been employed. Wilson has succesfully used load dependent Ritz vectors as an alternative for eigenvectors as a reduced basis in linear dynamic problems [26]. Van der Linde used these load dependent Ritz vectors in linear dynamics in combination with topology optimization [27]. Kanok-Nukulchai claims in his work [28] that load dependent Ritz vectors can also be used in nonlinear static problems, but he doesn't treat it in much detail. In the present work we try to use load dependent Ritz vectors as a reduced basis in nonlinear static problems, in combination with topology optimization.

4.2 LOAD DEPENDENT RITZ VECTORS

The mode superposition of load dependent Ritz vectors can be looked upon as a special case of the Rayleigh-Ritz method [29], in which the mode shapes are the Ritz vectors employed in the transformation of the original system. Within the context of the Rayleigh-Ritz method, it is not necessary to employ the very restrictive eigenvectors to discretize the system which lead to an uncoupled set of equations [30]. Load dependent Ritz vectors, or simply called "Ritz vectors" are therefore an alternative to eigenvectors. They are cheaper to compute and give a good representation of the spatial distribution of the applied load. To understand what Ritz vectors are and how they can be computed, we will first look at eigenvectors and Ritz vectors in linear dynamics, because this is where they originate from. Afterwards we make the step to nonlinear statics.

4.2.1 LINEAR DYNAMICS

EIGENVECTORS

To compute the eigenmodes of a system, the Arnoldi algorithm is frequently used [31]. Here the basis $\mathbf{V}$ forms the subspace in which the eigenvectors will be looked for using the Lanczos method. The Arnoldi algorithm consists of multiplying an arbitrary starting vector $\mathbf{v}_1$ with the dynamic flexibility matrix $\mathbf{K}^{-1}\mathbf{M}$ repeatedly, resulting in the Krylov sequence:

$$\mathbf{V} = \text{Span}\{\mathbf{v}_1, \mathbf{K}^{-1}\mathbf{M}\mathbf{v}_1, (\mathbf{K}^{-1}\mathbf{M})^2\mathbf{v}_1, (\mathbf{K}^{-1}\mathbf{M})^3\mathbf{v}_1, \ldots, (\mathbf{K}^{-1}\mathbf{M})^n\mathbf{v}_1\}. \tag{4.2}$$

Here $\mathbf{M}$ is the mass matrix and n the size of the reduced system. In contrast to the power iteration method, the subspace will not converge towards the first eigenvector, because all subsequent vectors are orthogonalized.

RITZ VECTORS

For the generation if Ritz vectors the same Arnoldi algorithm is used, but now the first vector is not arbitrary, but the static displacement:

$$\mathbf{v}_1 = \mathbf{K}^{-1}\mathbf{f}. \tag{4.3}$$

The vectors created using Equation 4.2 are the Ritz vectors. These Ritz vectors have a clear physical interpretation. The first Ritz vector, the static displacement, is multiplied by the mass matrix, yielding the associated inertia forces. The displacement caused by these forces is approximated by multiplying by the inverse of the stiffness matrix. The result is the new Ritz vector, and so on [27].

4.2.2 RITZ VECTORS IN NONLINEAR STATICS

In nonlinear statics, the same Arnoldi algorithm can be used as in linear dynamics. But now the stiffness matrix $\mathbf{K}$ becomes the tangent stiffness matrix $\mathbf{K}$ because it changes over time. The mass matrix $\mathbf{M}$ becomes the identity matrix $\mathbf{I}$, because inertia is neglected, and the external force $\mathbf{f}$ becomes the residual force $\mathbf{r}$. The first Ritz vector is the initial incremental displacement which shall serve as the load vector for the generation of subsequent Ritz vectors:

$$\mathbf{v}_1 = \mathbf{K}^{-1}\mathbf{r}, \tag{4.4}$$

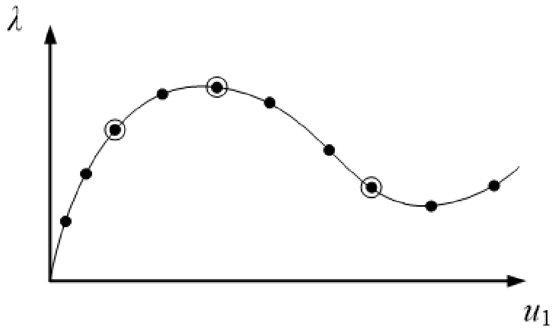

Figure 4.2: Equilibrium positions where the tangent stiffness matrix is updated (dots) and where the basis is updated (circles).

$$\mathbf{V} = \mathrm{Span}\{\mathbf{v}_1, \mathbf{K}^{-1}\mathbf{v}_1, (\mathbf{K}^{-1})^2\mathbf{v}_1, (\mathbf{K}^{-1})^3\mathbf{v}_1, \ldots, (\mathbf{K}^{-1})^n\mathbf{v}_1\}. \tag{4.5}$$

Each newly generated Ritz vector will be normalized with all previous Ritz vectors. In Figure 4.3 the physical interpretation of the Ritz vectors is explained using a simple problem of a cantilever beam. Each newly generated Ritz vector serves as a load system for subsequent Ritz vector. In between, the Ritz vectors are normalized and orthogonalized, but this does not change the space spanned by the basis.

REDUCED MODEL

Using the reduced basis, the reduced stiffness matrix $\tilde{\mathbf{K}}$ and the reduced residual force $\tilde{\mathbf{r}}$ can be computed:

$$\tilde{\mathbf{K}} = \mathbf{V}^{\mathrm{T}}\mathbf{K}\mathbf{V}, \tag{4.6}$$

$$\tilde{\mathbf{r}} = \mathbf{V}^{\mathrm{T}}\mathbf{r}. \tag{4.7}$$

The Newton-Raphson procedure can now be carried out with a reduced number of variables, to compute the reduced incremental displacements $\Delta\tilde{\mathbf{u}}$. The computational costs are reduced because the reduced stiffness matrix has less degrees of freedom than the full stiffness matrix. Both the stiffness matrix and the internal force have to be set up in the original system. Afterwards they can be transformed to the reduced system using Equations 4.6 and 4.7.

Both the tangent stiffness matrix and the residual force vector are subjected to continuous change, thus the basis should be updated. An example is given in Figure 4.2. Either the full or modified Newton-Raphson scheme can be used. However, the full Newton-Raphson scheme is preferred, because here the reduction method can be exploited more by frequently inverting the stiffness matrix, with low computational costs. When using the modified Newton-Raphson scheme there is less need to transform the stiffness matrix, because the old full stiffness matrix has already been inverted.

An advantage of Ritz vectors over eigenvectors is that the spatial distribution of the applied load is represented very well. A possible disadvantage is that correction steps in the incremental-iterative procedure are usually related to high stiffness modes. These modes are perhaps not included in the Ritz vector basis. Also, a Ritz vector basis is not a smart choice in the presence of buckling, because in a bifurcation point, the applied load is orthogonal to the displacement field. see Equation 2.23.

4.2.3 COMPLETENESS OF THE BASIS

It is assumed that the full system is of size N, which means it has N degrees of freedom. If N eigenvectors are included in a modal basis, the basis is complete and it represents the original problem exactly. A question that arises, is whether this is also the case for a Ritz vector basis. In other words, can Ritz vectors be used to generate a full basis and what happens if we keep on multiplying with $\mathbf{K}^{-1}$ in the Krylov sequence after the N'th Ritz vector is generated?

In some cases it is possible to generate a full basis. When N linearly independent Ritz vectors are generated, the entire space $\mathbb{R}^N$ can be spanned. When Ritz vector $N+1$ is generated, this will always be a linear combination of the first N Ritz vectors. However, it is not yet clear when the Ritz vectors will be linearly independent, and if so, how many of them. This section will provide a derivation of how many basis vectors can be generated.

Let κ_i be the eigenvalues of the tangent stiffness matrix and $\boldsymbol{\phi}_i$ the eigenvectors, $i = 1,2,\ldots N$. They are the modal stiffnesses and the eigenmodes respectively. The eigenmodes are normalized such that $\boldsymbol{\phi}_i \cdot \boldsymbol{\phi}_i = 1$. Let the columns of the modal matrix $\boldsymbol{\Phi}$ be the eigenmodes, i.e. $\boldsymbol{\Phi} = [\boldsymbol{\phi}_1 \;\; \boldsymbol{\phi}_2 \;\; \ldots \;\; \boldsymbol{\phi}_N]$. Since $\boldsymbol{\Phi}$ is an orthonormal basis, the following important relation holds: $\boldsymbol{\Phi}^\top\boldsymbol{\Phi} = \mathbf{I}$, so $\boldsymbol{\Phi}^{-1} = \boldsymbol{\Phi}^\top$. The modal matrix is used to transform the residual force and the stiffness matrix to a modal basis:

$$\mathbf{r} = \boldsymbol{\Phi}\mathbf{q}, \tag{4.8}$$

$$\mathbf{K} = \boldsymbol{\Phi}\boldsymbol{\kappa}\boldsymbol{\Phi}^\top. \tag{4.9}$$

Where $\mathbf{q}$ is a vector containing the modal loads and $\boldsymbol{\kappa}$ is the modal stiffness matrix:

$$\boldsymbol{\kappa} = \boldsymbol{\Phi}^\top\mathbf{K}\boldsymbol{\Phi} = \mathrm{Diag}[\kappa_1,\ \kappa_2,\ \ldots,\ \kappa_N]. \tag{4.10}$$

The modal stiffnesses are ordered such that $\kappa_i \leq \kappa_{i+1}$. The first Ritz vector can be expressed in terms of the modal basis:

$$\begin{aligned}
\mathbf{v}_1 &= \mathbf{K}^{-1}\mathbf{r} \\
&= \left(\boldsymbol{\Phi}\boldsymbol{\kappa}\boldsymbol{\Phi}^\top\right)^{-1}\boldsymbol{\Phi}\mathbf{q} \\
&= \boldsymbol{\Phi}\boldsymbol{\kappa}^{-1}\boldsymbol{\Phi}^\top\boldsymbol{\Phi}\mathbf{q} \\
&= \boldsymbol{\Phi}\boldsymbol{\kappa}^{-1}\mathbf{q} \\
&= \boldsymbol{\Phi}\begin{bmatrix} q_1/\kappa_1 \\ q_2/\kappa_2 \\ \vdots \\ q_N/\kappa_N \end{bmatrix}.
\end{aligned} \tag{4.11}$$

In the same way it can be shown that the second Ritz vector can written as

$$\mathbf{v}_2 = \boldsymbol{\Phi}\boldsymbol{\kappa}^{-2}\mathbf{q} = \boldsymbol{\Phi}\begin{bmatrix} q_1/\kappa_1^2 \\ q_2/\kappa_2^2 \\ \vdots \\ q_N/\kappa_N^2 \end{bmatrix}. \tag{4.12}$$

Before the third Ritz vector is generated, the second Ritz vector has to be orthogonalized with respect to the first Ritz vector. However, this orthogonalization process does not change the space spanned by the first two Ritz vectors. The n'th Ritz vector becomes

$$\mathbf{v}_n = \boldsymbol{\Phi}\boldsymbol{\kappa}^{-n}\mathbf{q} = \boldsymbol{\Phi}\begin{bmatrix} q_1/\kappa_1^n \\ q_2/\kappa_2^n \\ \vdots \\ q_N/\kappa_N^n \end{bmatrix}. \tag{4.13}$$

From Equation 4.13 it can be concluded that only the eigenmodes that are excited by the external force (and thus also the residual force) are included in the Ritz vector basis. For example, when the i'th

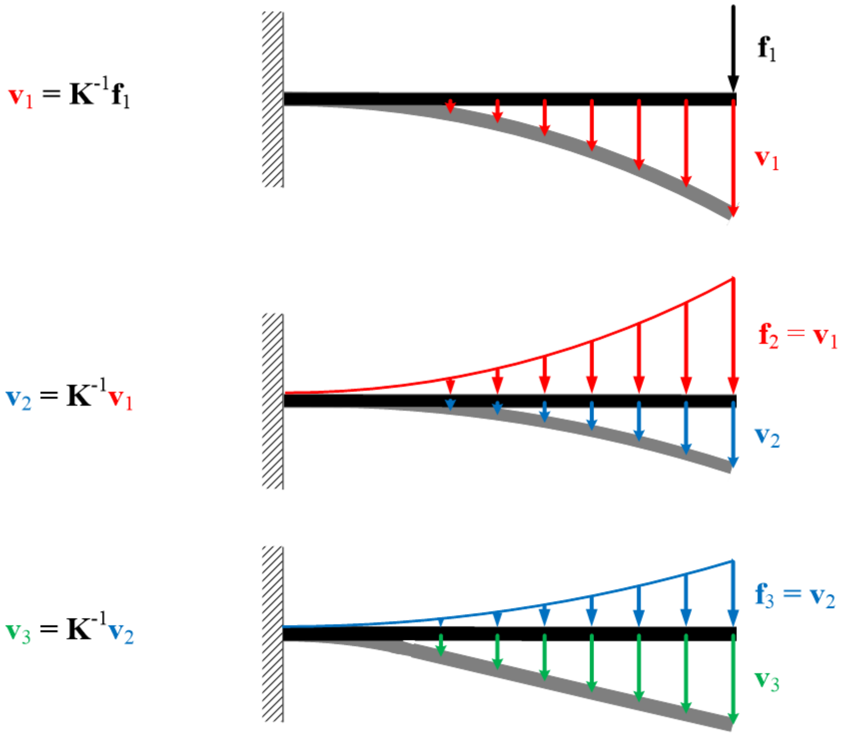

Figure 4.3: Physical interpretation of the load dependent Ritz vectors. The load system $\mathbf{f}_1$ causes a displacement field $\mathbf{v}_1$, which is the first Ritz vector. This displacement field serves as a new load system $\mathbf{f}_2$, which results in a new displacement field $\mathbf{v}_2$, which is the second Ritz vector, and so on.

eigenmode is not excited by the external force, then $q_i = 0$, and the i'th column of $\mathbf{\Phi}$ is not selected. This means that the maximum number of linearly independent Ritz vectors that can be included in the basis, is equal to the number of eigenmodes excited by the external force.

This mathematical derivation can also be explained from a more physical point of view using the example in Figure 4.3. Axial deformation modes are obviously not excited by the external force $\mathbf{f}_1$. As a result, these modes will not be included in the basis. This becomes problematic when we want to represent finite displacements using this basis. For large magnitudes of $\mathbf{f}_1$, the beam will bend considerably and the tip will displace to the left. Since this contains an axial deformation mode, this displacement cannot be described using the Ritz vector basis.

This problem is not restricted to a Ritz vector basis, but does also occur when one would use an eigenvector basis. In the latter case, normally the modes with the lowest modal stiffnesses are chosen, which are in this example lateral deformation modes. In advance, it is not known which eigenmode corresponds to the stiff axial deformation, so it is difficult to include it in the modal basis.

It is concluded that the load dependent Ritz vector reduced model will in general not lead to accurate results. Therefore, the topology optimization problems in this work will be carried out without the use of a reduction method. One of the existing reduction methods can be implemented in future work to reduce the computational costs.

5

MINIMIZATION OF END-COMPLIANCE

The most widely used methods for structural topology optimization can be classified as density-based methods. Density-based methods operate on a fixed domain of finite elements with the goal of minimizing an objective function by identifying whether each element should consist of solid or void material.

5.1 PROBLEM FORMULATION

It is desirable to replace the discrete variables with continuous variables such that gradient-based algorithms can be used. This is accomplished with an interpolation function, where the continuous design variables are explicitly interpreted as the material density of each element. In the present work the popular Solid Isotropic Material with Penalization (SIMP) method [32] is used. In this method the constitutive matrix is scaled with the element density:

$$\mathbf{D} \quad \longrightarrow \quad \rho_e^p \mathbf{D}. \tag{5.1}$$

The penalization parameter p is used to make intermediate densities unfavourable. A low value of p results in more intermediate density elements, while a high value of p results in a less convex optimization problem. Usually $p = 3$ is a good value [33].

Instead of scaling the constitutive matrix, the tangent stiffness matrix and the internal force vector can be scaled separately, because they are linear in the scaling factor ρ_e^p. Scaling the stiffness matrix is done because this implementation resembles the implementation of topology optimization of linear mechanics problems. This has the advantage that the element stiffness matrices only have to be constructed once. After the analysis, the stress field should be multiplied with the penalized density field to obtain the correct stresses:

$$\rho_e^p \mathbf{K}_e = \rho_e^p \left(\mathbf{B}^\top \mathbf{D} \mathbf{B} + \mathbf{G}^\top \mathbf{S} \mathbf{G} \right), \tag{5.2}$$

$$\rho_e^p \mathbf{f}_{\text{int}}^e = \rho_e^p \mathbf{B}^\top \boldsymbol{\sigma}, \tag{5.3}$$

where

$$\boldsymbol{\sigma} = \mathbf{D} \boldsymbol{\varepsilon}. \tag{5.4}$$

The general formulation of a topology optimization problem based on nonlinear static finite element analysis may be given as

$$
\begin{aligned}
\min_{\boldsymbol{\rho}} \quad & f(\lambda, \mathbf{u}, \boldsymbol{\rho}) \\
\text{s.t.} \quad & \mathbf{r}(\lambda, \mathbf{u}, \boldsymbol{\rho}) = \mathbf{0}, \\
& \sum_{e=1}^{n_{\mathrm{el}}} \rho_e V_e - V^* \leq 0, \\
& 0 < \rho_{\min} \leq \rho_e \leq 1, \qquad (e = 1, 2, \ldots, n_{\mathrm{el}}).
\end{aligned}
\tag{5.5}
$$

In contrast to linear problems, the objective function f is not only a function of the displacement field $\mathbf{u}$ and the densities $\boldsymbol{\rho}$, but also of the load parameter λ. Moreover, in nonlinear problems equilibrium is not automatically satisfied. Therefore, a constraint is incorporated that states that the residual force should be zero within a specified tolerance. The amount of material is constrained by a maximum volume V^*. The densities range from 0 to 1, where 0 corresponds to a void element (white) and 1 to a solid element (black). $\rho_{\min} = 10^{-3}$ is the minimum density, which is required to prevent difficulties associated with zero values, such as singular finite element matrices.

FILTERING

Two other issues that arise are checkerboarding and mesh dependent designs. Both problems are solved by applying an distance weighted average filter. This is a blurring filter which effectively restricts the minimum feature size to the filter radius [34]. The filtered densities $\hat{\boldsymbol{\rho}}$ are obtained by multiplying the densities by a filter matrix $\mathbf{A}$:

$$\hat{\boldsymbol{\rho}} = \mathbf{A}\boldsymbol{\rho}. \tag{5.6}$$

The filtering step influences the sensitivities and this will be discussed in Section 5.3.1.

It was observed that the filter does not work as good as expected when using a structured triangular mesh. The reason for this is that some neighbouring elements fall within the radius, while other neighbouring elements do not. For this reason an unstructured mesh is used.

OPTIMAL MICROSTRUCTURE

In the homogenization approach an optimal orthotropic microstructure is oriented in the direction of the principal stresses. This provides a bound for the structural performance. In the case of finite displacements, the existence of optimal microstructures has not been proven so far. However, an early paper by Michell [35] states that the optimal microstructure should remain orthogonal throughout the deformation history.

METHOD OF MOVING ASYMPTOTES

The method of moving asymptotes (MMA) by Svanberg [36] is chosen as optimization algorithm. MMA is generally used in topology optimization because of its fast convergence and ability to deal with a large number of design variables. A move limit of 0.2 is imposed on the design variables in an attempt to limit intermediate densities in the design. MMA is a gradient-based algorithm, which means sensitivity information of the design is required. This is derived in Section 5.3.

OBJECTIVE FUNCTIONS

The objective in this optimization problem is to minimize the compliance of the structure, or in other words, to maximize the stiffness. Since the problem is nonlinear, the stiffness is not uniquely defined and depends on the load intensity. Minimizing the displacements under the final load is called end-compliance minimization. The corresponding objective function is

$$C = f_{\mathrm{EC}} = \mathbf{f}_{\mathrm{ext}}^{\top}(\lambda)\,\mathbf{u}(\lambda, \boldsymbol{\rho}). \tag{5.7}$$

Other possibilities for generating stiff structures are to minimize the strain energy:

$$f_{\mathrm{SE}} = \tfrac{1}{2} \int_V \boldsymbol{\varepsilon}^\top \boldsymbol{\sigma} \, \mathrm{d}V, \tag{5.8}$$

or the complementary work:

$$f_{\mathrm{CW}} = \int_0^{\lambda_{\mathrm{end}}} f_{\mathrm{EC}} \, \mathrm{d}\lambda. \tag{5.9}$$

Note that in linear mechanics problems the above-mentioned objective functions are equivalent and lead to the same design. In the present work the end-compliance will be used because of its simplicity and its resemblance to linear compliance minimization.

5.2 MESH DISTORTION

A big problem in density-based topology optimization of geometrically nonlinear structures is mesh distortion. Due to excessive deformation in low stiffness areas, low density elements get crushed and become unstable. This phenomena may lead to nonconvergence on the equilibrium equations, because the tangent stiffness matrix becomes indefinite or even negative definite. The reason for this is that the Green-Lagrange strain is based on the deformation gradient and is only physically meaningful when a body is not turned inside out, associated with negative volume [37]. The computed strains, stresses and internal forces are thus no longer physically meaningful. These local instabilities must not be confused with global instabilities of the structure such as buckling and limit-load behavior, because these can be captured by the mechanical analysis. In linear analysis, the abnormal deformation is not a critical matter because the deformation is never further used.

Different approaches have been proposed to solve this problem. A lot of them are summarized in [38], but they have drawbacks or cannot completely solve the problem. For example, the convergence tolerance for the degrees of freedoms of elements which exhibit unstable behavior can be relaxed, but this reduces the accuracy of the solution and, therefore, affects the sensitivities. Another approach would be to remove void elements. However, instabilities can also arise in low density elements and other elements might get disconnected from the remainder of the structure. Another proposed method is to use a linear strain measure for void elements and a nonlinear strain measure for solid elements. However, this needs to be tuned separately for different types of problems. Also remeshing can be done, but this is computationally expensive and will introduce numerical noise in the response due to the changing discretization.

All previous methods are based on scaling material properties. As an alternative, Yoon and Kim [39] introduced an alternative design interpolation method called the Element Connectivity Parameterization. Void elements can be disconnected from their neighbors by scaling the stiffness of one-dimensional linear springs between the element degrees of freedom. Unfortunately, also here local instabilities can arise at severe deformations. Another new design interpolation scheme is proposed in [38], called Element Deformation Scaling. Instead of scaling the internal force (via de the stiffness), the displacements are scaled. But also this method does not always perform well at severe deformations. Finally, another interpolation scheme is proposed in [40] which adds a hyperelastic material to the design domain to prevent excessive deformation. It has however not been proven that the approximation of the remodeled structure is sufficiently accurate.

The examples in this work will be carried out without any measures to prevent mesh distortion. Hereby, we can determine how severe this effect is. It is expected that for 2D examples mesh distortion becomes problematic when very large loads are applied. On the other hand, for shell structures the effect is expected to be limited, since these structures mainly deform out of plane. However, the global tangent stiffness matrix will be ill-conditioned, because of the assembled penalized solid and void elements in combination with high membrane stiffnesses and low bending stiffnesses. This will also cause convergence difficulties, especially for thin shells.

5.3 SENSITIVITIES

Since topology optimization uses many design variables, the use of gradient-based optimization algorithms is inevitable. These algorithms require the sensitivities of the response functions (objective and constraints). In contrast to many material nonlinearities, geometrically nonlinear problems are path independent. An exception are problems in which bifurcation occurs. In this case the structure might follow another path during unloading than during loading. In the present work bifurcation problems will not be considered. If the problem is path-independent, no backward integration is needed to calculate the sensitivities. In the following section, the sensitivities of the end-compliance minimization problem are derived. However, a large part of this derivation can also be used for determining the sensitivities of structures that follow a prescribed equilibrium path, as will be presented in Chapter 6.

5.3.1 ADJOINT SENSITIVITIES

The sensitivity is the derivative of the objective function C in Equation 5.7 with respect to the density of element e. If the applied load is independent of the design, this yields to

$$\frac{\partial C}{\partial \rho_e} = \mathbf{f}_{\text{ext}}^{\top} \frac{\partial \mathbf{u}}{\partial \rho_e}. \tag{5.10}$$

Unfortunately, this involves computing the state sensitivity $\partial \mathbf{u}/\partial \rho_e$, which is computationally very expensive because the displacements have to be computed for a perturbation of every design variable ρ_e. This means that the number of nonlinear finite element analyses that has to be carried out, is equal to the number of elements. To circumvent this computation, the adjoint term $\boldsymbol{\mu}^{\top}\mathbf{r}$ is added to the objective function:

$$C = \mathbf{f}_{\text{ext}}^{\top}\mathbf{u} + \boldsymbol{\mu}^{\top}\mathbf{r}. \tag{5.11}$$

Here $\boldsymbol{\mu}$ is the vector of the adjoint variables or Lagrange multipliers and $\mathbf{r}$ is the residual force. Assuming that the structure is in equilibrium, the residual force is zero and the objective function remains unchanged. This holds for every value of $\boldsymbol{\mu}$. The residual force is both a direct and an indirect function of the density (via the displacement), so the modified sensitivity function is

$$\frac{\partial C}{\partial \rho_e} = \mathbf{f}_{\text{ext}}^{\top} \frac{\partial \mathbf{u}}{\partial \rho_e} + \boldsymbol{\mu}^{\top} \left(\frac{\partial \mathbf{r}}{\partial \mathbf{u}} \frac{\partial \mathbf{u}}{\partial \rho_e} + \frac{\partial \mathbf{r}}{\partial \rho_e} \right). \tag{5.12}$$

The goal is to choose the right value for $\boldsymbol{\mu}$, such that the state sensitivity is eliminated. Therefore, Equation 5.12 is rearranged with the state sensitivity factored out:

$$\frac{\partial C}{\partial \rho_e} = \left[\mathbf{f}_{\text{ext}}^{\top} + \boldsymbol{\mu}^{\top} \frac{\partial \mathbf{r}}{\partial \mathbf{u}} \right] \frac{\partial \mathbf{u}}{\partial \rho_e} + \boldsymbol{\mu}^{\top} \frac{\partial \mathbf{r}}{\partial \rho_e}. \tag{5.13}$$

In order to make the first term equal to zero, the adjoint variables should chosen as

$$\boldsymbol{\mu} = - \left[\frac{\partial \mathbf{r}}{\partial \mathbf{u}} \right]^{-\top} \mathbf{f}_{\text{ext}} = \mathbf{K}^{-1} \mathbf{f}_{\text{ext}}, \tag{5.14}$$

where we make use of the fact that $-\partial \mathbf{r}/\partial \mathbf{u}$ is the tangent stiffness matrix $\mathbf{K}$ and that $\mathbf{K}$ is symmetric. The computation of the adjoint variables requires only one additional backward substitution, because the tangent stiffness matrix has already been factorized during the objective function evaluation, i.e: during the nonlinear finite element analysis. Obtaining the sensitivity information using the adjoint method is thus computationally cheap, especially compared to the objective function evaluation.

The part that still has to be computed is the sensitivity of the residual. The residual is the difference between the external and internal force. Since the external force is independent of the design, its derivative with respect to the densities is zero. This means that the sensitivity of the residual is equal to minus the sensitivity of the internal force. Using Equation 2.5 and Equation 2.6, the internal force on element level can be expressed as

$$\mathbf{f}_{\text{int},e} = \int_{V_e} \mathbf{B}^\top \boldsymbol{\sigma} \, \mathrm{d}V_e = \int_{V_e} \mathbf{B}^\top \rho_e^p \mathbf{D} \boldsymbol{\varepsilon} \, \mathrm{d}V_e. \tag{5.15}$$

The sensitivity of the residual on element level is thus

$$\frac{\partial \mathbf{r}_e}{\partial \rho_e} = -\frac{\partial \mathbf{f}_{\text{int},e}}{\partial \rho_e} = -\int_{V_e} \mathbf{B}^\top p \rho_e^{p-1} \mathbf{D} \boldsymbol{\varepsilon} \, \mathrm{d}V_e. \tag{5.16}$$

One may argue that the deformation is also a function of the density via the displacement, i.e. $\boldsymbol{\varepsilon}(\mathbf{u}(\rho))$. However, this dependency has already been taken into account in Equation 5.12 where the chain rule is applied. It is important to note that in order to obtain accurate sensitivities, the analysis must be solved accurately. Since one of the basic assumptions is $\mathbf{r} = 0$, a small tolerance should be used during the Newton-Raphson process. In conclusion, we can say that the sensitivity of the end-compliance minimization problem is

$$\frac{\partial C}{\partial \rho_e} = \boldsymbol{\mu}^\top \frac{\partial \mathbf{r}}{\partial \rho_e}, \tag{5.17}$$

where $\boldsymbol{\mu}$ can be computed using Equation 5.14 and $\partial \mathbf{r} / \partial \rho_e$ using Equation 5.16 after assembling.

FILTERING STEP

When a filtering step is applied, this influences the sensitivities. Since the response is based on the filtered densities $\hat{\boldsymbol{\rho}}$, the sensitivities are also based on the filtered densities. In this case, Equation 5.17 becomes

$$\frac{\partial C}{\partial \hat{\rho}_e} = \boldsymbol{\mu}^\top \frac{\partial \mathbf{r}}{\partial \hat{\rho}_e}. \tag{5.18}$$

However, we want to know the sensitivities with respect to the unfiltered densities $\boldsymbol{\rho}$, since these are the design variables. Applying the chain rule and using Equation 5.6 gives

$$\frac{\mathrm{d}C}{\mathrm{d}\boldsymbol{\rho}} = \frac{\partial C}{\partial \hat{\boldsymbol{\rho}}} \frac{\partial \hat{\boldsymbol{\rho}}}{\partial \boldsymbol{\rho}} = \frac{\partial C}{\partial \hat{\boldsymbol{\rho}}} \mathbf{A} = \mathbf{A}^\top \frac{\partial C}{\partial \hat{\boldsymbol{\rho}}}. \tag{5.19}$$

The filter correction thus yields a multiplication with the filter matrix.

5.3.2 FINITE DIFFERENCE SENSITIVITIES

An alternative for adjoint sensitivities are finite difference sensitivities. For nonlinear problems they can be obtained relatively cheap by making use of the fact that the perturbed equilibrium path is very similar to the nominal equilibrium path, see Figure 5.1. However, for problems containing many design variables this is still more expensive than adjoint sensitivities. In the case of topology optimization this means that at least one system of linear equations has to be solved for every element, while for adjoint sensitivities this has to be done for every response function. For this reason, the optimization is performed using adjoint sensitivities, but finite differences are used to check the whether these values are correct. This is done for six arbitrary elements during the first design iteration of the cantilever problem that will be discussed in Section 5.4.1. A central finite difference scheme is used with a perturbation of $\Delta\rho_e = 10^{-3}$:

$$\frac{\partial C}{\partial \rho_e} = \frac{C(\lambda, \mathbf{u}, \rho_e + \Delta\rho_e) - C(\lambda, \mathbf{u}, \rho_e - \Delta\rho_e)}{2\Delta\rho_e}. \tag{5.20}$$

The values are compared in Table 5.1. In the iterative analysis a force norm of 10^{-3} was used. The relative differences have an order of magnitude of 10^{-8}. Therefore it can be concluded that the adjoint sensitivities are correct.

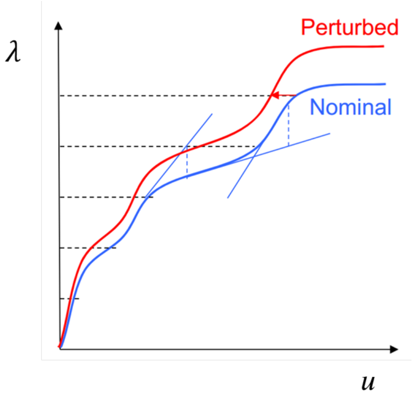

Figure 5.1: When using finite differences, the perturbed equilibrium path deviates slightly from the nominal equilibrium path. The iterations can therefore be started from unperturbed solution and no full analysis is necessary. [41]

Table 5.1: Comparison of adjoint sensitivity value and finite difference sensitivity value for six arbitrary elements.

Element number	Adjoint sensitivity value	Finite difference sensitivity value	Relative difference
1125	-1.53×10^{-6}	-1.53×10^{-6}	-2.51×10^{-8}
71	-1.60×10^{-6}	-1.60×10^{-6}	-2.52×10^{-8}
686	-1.74×10^{-6}	-1.74×10^{-6}	-2.44×10^{-8}
123	-2.90×10^{-6}	-2.90×10^{-6}	-3.01×10^{-9}
1745	-1.54×10^{-6}	-1.54×10^{-6}	-2.47×10^{-8}
10	-2.00×10^{-7}	-2.00×10^{-7}	-1.97×10^{-8}

5.4 EXAMPLES OF 2D STRUCTURES

In this section end-compliance minimization will be applied on two simple 2D design problems, to study the effectiveness of this method. Load control is used such that we can easily prescribe the load intensity for which we want to optimize the structure. In addition, one load increment proved to be sufficient to obtain convergence in the equilibrium equations.

5.4.1 CANTILEVER

The first problem is a simple cantilever. Since the objective function is

$$f = \mathbf{u}^\top \mathbf{f}_{\text{ext}}, \tag{5.21}$$

the vertical displacement of the point where the load is applied is to be minimized. The design domain is given in Figure 5.2a and is discretized using three-noded triangular elements. Details of the problem are provided in the caption. The optimization process is started from a homogeneous density distribution. The optimal design that was obtained using linear analysis is shown in Figure 5.2b and is independent of the load intensity. When this "linear design" is analyzed using nonlinear analysis, it performs quite well for large loads, as can be seen in Figure 5.2c. The vertical displacement of the point where the load is applied is $u = 0.45\,\text{m}$. For comparison, the initial design is analyzed nonlinearly in Figure 5.2d and has a displacement of $u = 1.28\,\text{m}$.

The optimal design that is obtained using nonlinear analysis is shown in Figure 5.2e and is regarded as the "nonlinear design". It is observed that this design is different from the linear design. At first sight the design might not look like the optimal solution, but the topology makes sense when looking at the deformed configuration in Figure 5.2f. The member on the right side of the structure that directly supports the load, is near vertical in the deformed configuration. This results in the member being loaded in pure tension and therefore the structure is very stiff. The vertical displacement is $u = 0.43\,\text{m}$ which is slightly smaller than the endpoint displacement of the linear design. For smaller load intensities, the member on the right will be loaded in bending and the structure performs worse. The optimization was performed for different load intensities. It was concluded that the design obtained using nonlinear analysis differs more from the design obtained using linear analysis as the load intensity increases. The nonlinear design is only optimal for the load intensity it is optimized for.

The Newton-Raphson procedure in combination with load control and one load increment is used to carry out the nonlinear analyses. In Figure 5.3 the number of equilibrium iterations versus the number of design iterations is plotted. In the beginning the Newton-Raphson procedure has difficulties to converge because the displacements are large and mesh distortion occurs. In the end the algorithm manages to converge in approximately 15 equilibrium iterations. The objective function value also steadily decreases along with the number of equilibrium iterations. The optimization process is terminated based on the relative change in the objective function value. Since this is not a very good criterion, the process is continued manually for a fixed number of iterations. A better approach would be to terminate the process based on KKT-conditions [42]. This feature could be added in future work.

5.4.2 DOUBLE CLAMPED STRUCTURE

The next example demonstrates that topology optimization based on linear and nonlinear modeling can give a completely different result. The design problem of the double clamped structure is shown in Figure 5.4a. The optimal design obtained using linear analysis is rather simple, as can be seen in Figure 5.4b. It consists of two members which are mainly loaded in compression, and looks therefore very stiff. However, for large loads the members can buckle and snap-through occurs.

When the optimization is performed based on nonlinear analysis, the optimal design is entirely different, as can be seen in Figure 5.4d. The structure now consists of two long members loaded in tension to prevent buckling. The two members in the middle which are loaded in compression are shorter and more vertical such that they are less sensitive to buckling. A small asymmetry can

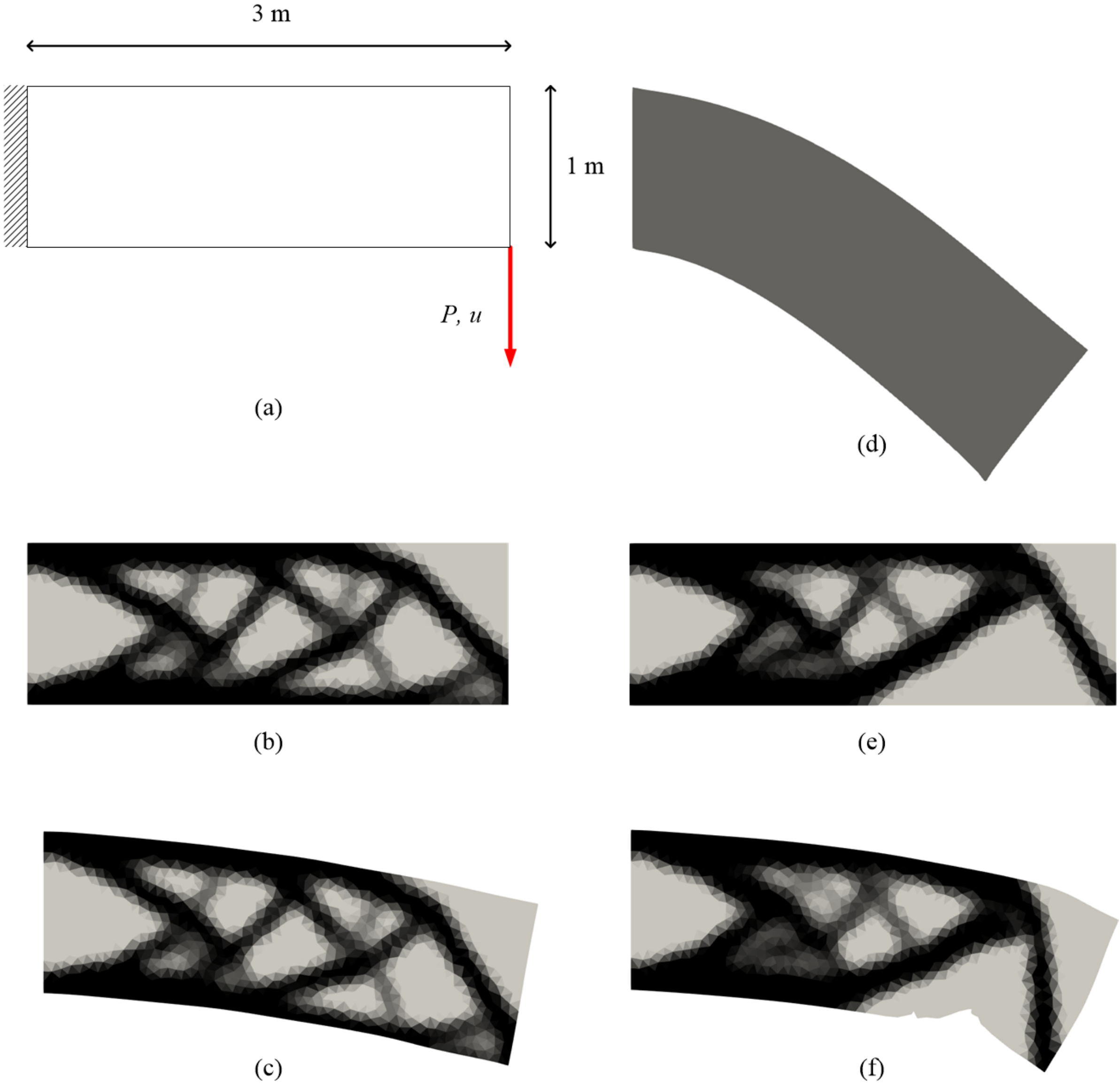

Figure 5.2: Topology optimization problem of the cantilever. Displacements are not scaled. $P = 4\,\text{kN}$, $V^* = 0.5$, $n_{\text{el}} = 1907$, $E = 200\,\text{MPa}$, $\nu = 0.3$ and $h = 0.01\,\text{m}$. (a) Design domain. (b) Optimal design obtained using linear analysis. (c) Linear design analyzed using nonlinear analysis, $u = 0.45\,\text{m}$. (d) Deformed configuration of the homogeneous initial design, $u = 1.28\,\text{m}$. (e) Optimal design obtained using nonlinear analysis. (f) Deformed configuration of the nonlinear design, $u = 0.43\,\text{m}$.

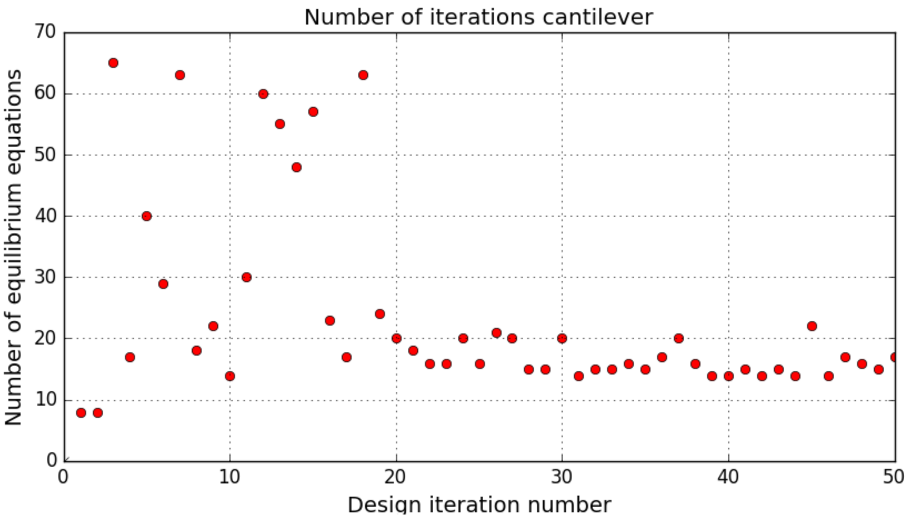

Figure 5.3: Number of equilibrium iterations for every design iteration for the cantilever problem. A force norm of 10^{-5} is used as convergence criterion.

be observed in the nonlinear design, which is caused by the asymmetric mesh. Although the design problem is symmetric, assymetric solutions, such as snap-through modes, exist when the structure is analyzed using nonlinear analysis. Therefore, analyzing only half of the (symmetric) structure is not a good approach.

The nonlinear design seems like a well performing design when keeping in mind buckling and snap-through effects. However, its performance is not as good as that of the linear design. When the nonlinear and linear designs are evaluated for the design load using nonlinear analysis, the displacements are $u = 22.5\,\text{mm}$ and $u = 2.4\,\text{mm}$ respectively. This is due to the fact that the applied load is relatively small and therefore no snap-through occurs in the linear design. The nonlinear design in Figure 5.4d is obtained because the displacements in the beginning of the design process are large. Therefore, the sensitivities steer the optimization process to this nonlinear design and the optimizer gets stuck in a local minimum. It is expected that when the linear design in Figure 5.4b is used as an initial condition for the nonlinear optimization process, it will result in the same design as the linear design. Furthermore, it is expected that for large loads the nonlinear design in Figure 5.4d is superior, but this could not be tested due to mesh distortion. In conclusion we can say, that even for small loads, topology optimization based on nonlinear analysis can result in designs that perform well under large loads. Partly this is because nonlinear effects are taken into account, but also partly because of the inability of the optimizer to find the global optimum.

5.5 EXAMPLES OF SHELL STRUCTURES

Nonlinearities play an important role in the failure of large shell structures, such as wind turbine blades, which primarily fail due to nonlinear effects [43]. It is therefore interesting to see if considering these nonlinear effects in topology optimization leads to different designs. Again, it proved to be sufficient to use load control with one load increment.

5.5.1 SQUARE PLATE

Starting simple, the optimization problem of a square plate is shown in Figure 5.5. The top and left edges are fixed and an out of plane force is applied in the lower right corner. Although the displacements are relatively large, the linear and nonlinear analysis yield the same design. This is not surprising, because this design results in the shortest load path.

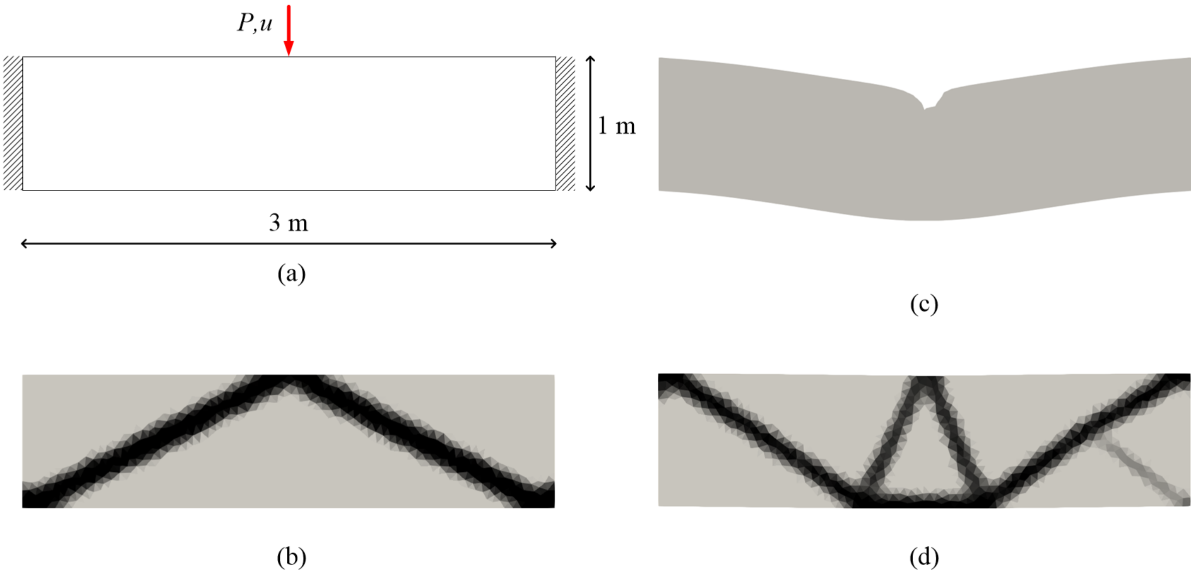

(a) (c) (b) (d)

Figure 5.4: Topology optimization problem of the double clamped structure. All designs are shown in their deformed configuration, but displacements are very small. $P = 250\,\mathrm{N}$, $V^* = 0.2$, $n_{\mathrm{el}} = 2588$, $E = 200\,\mathrm{MPa}$, $\nu = 0.3$ and $h = 0.01\,\mathrm{m}$. (a) Design domain. (b) Optimal design obtained using linear analysis, $u = 2.4\,\mathrm{mm}$. (c) Homogeneous initial design, $u = 14.4\,\mathrm{mm}$. (d) Optimal design obtained using nonlinear analysis, $u = 22.5\,\mathrm{mm}$.

The example becomes more interesting when the fixed supports are replaced by hinges, as shown in Figure 5.6a. The corner where the two hinges meet, acts as a fixed support, because the hinges counteract each other. Therefore, it is beneficial to place material in this corner, as can be seen for the linear design in Figure 5.6b. Because the mesh is not symmetric, the optimizer gets stuck in a local minimum that results in the asymmetric design. However, it is assumed that the optimal linear design consists of a square plate with several holes.

When the optimization is performed based on nonlinear analysis, the design is completely different, as can be seen in Figure 5.6e. It resembles the design of the fixed plate in Figure 5.5, and has no material at the fixed support in the corner. If the performance is compared, we see that the displacement of the homogeneous initial design at the corner where the load is applied is $u = 0.24\,\mathrm{m}$ (Figure 5.5d), the linear design $u = 0.11\,\mathrm{m}$ (Figure 5.5c) and the nonlinear design $u = 0.067\,\mathrm{m}$ (Figure 5.5f). Thus, the nonlinear design performs considerably better than the linear design (38%).

The differences between the linear and nonlinear design can be explained by looking at the stresses in the plate. We compare the von Mises stresses calculated using the linear and nonlinear model of the homogeneous initial design. The membrane stresses calculated using the linear model are zero, because the load is perpendicular to the plate in the undeformed configuration. The bending stresses calculated using the linear model are constant over the plate, because the applied boundary conditions lead to a constant twist (or warp) curvature, which is a measure for the bending stresses. Therefore, the total stress is constant over the plate (for a given distance from the midplane) and there is no pronounced preference for where to place material. This leads to the linear design in Figure 5.6b.

The membrane stresses for the initial homogeneous design calculated using the nonlinear model are shown in Figure 5.7a. The membrane stresses are nonzero, because the nonlinear model takes into account the deformed configuration. For the same reason, the bending stresses calculated using the nonlinear model are not constant, as shown in Figure 5.7b. If the membrane stresses are plotted using a colormap with a different scale (with a lower maximum value) in Figure 5.7c, the stress field resembles the density field in Figure 5.6e. Apparently, the membrane stresses have a large influence on the differences between the designs. It is also noticed that the plate displaces upward near the upper

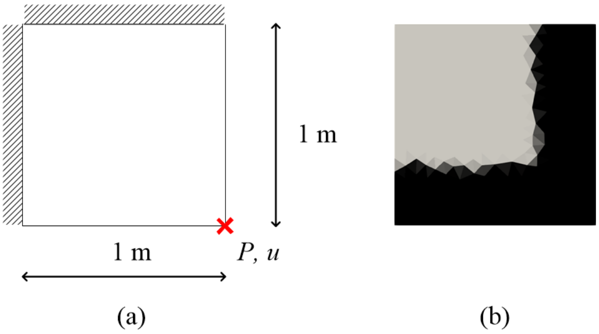

(a) (b)

Figure 5.5: Topology optimization problem of the fixed squire plate loaded out of plane. $P = 5\,\mathrm{N}$, $V^* = 0.5$, $n_{\mathrm{el}} = 585$, $E = 200\,\mathrm{MPa}$, $\nu = 0$ and $h = 0.01\,\mathrm{m}$. (a) Design domain. (b) The optimal design obtained using linear and nonlinear analysis is the same.

left corner resulting from the nonlinear model. This holds for the homogeneous initial design as well as for the first few design iterations. In Figure 5.7d this can clearly be seen for design iteration 4. This effect is not observed in linear analysis.

5.5.2 SPHERICAL SHELL

The last example presented in this work is the spherical shell shown in Figure 5.8a. The homogeneous initial design undergoes a very large deflection, as can be seen in Figure 5.8d. The linear and nonlinear design are shown in Figure 5.8b and Figure 5.8e respectively. Although these designs resemble each other, the deflection calculated using a nonlinear analysis of the nonlinear design is considerably smaller than the deflection of the linear design, as can be seen in Figure 5.8f and Figure 5.8c respectively. In terms of objective function, the nonlinear design performs 35% better than the linear design and 79% better than the initial homogeneous design.

For very thin shells it is extremely difficult to obtain convergence in the equilibrium equations. This is due to the ill-conditioning of the tangent stiffness matrix which contains high membrane stiffness terms and low bending stiffness terms. The multiplication of these terms with high and low penalized densities deteriorates the conditioning even further. A small increase of the thickness alleviates this problem.

5.6 DISCUSSION

The cantilever and the double clamped structure did suffer from mesh distortion. However, convergence was achieved, despite the large number of equilibrium equations that was required. A possible explanation for this is that the entire load is applied at once and that there is no restriction on the iterative displacement. Apparently, this gives the Newton-Raphson process the opportunity to skip difficult parts of the equilibrium path. The use of smaller load increments or a more advanced path-following technique such as arc-length control, will most likely result in more convergence difficulties. In these examples, it was not possible to achieve convergence for loads much higher than the loads that are applied here.

An interesting observation is that in all found literature (see Section 5.2), topology optimization was performed using a structured mesh consisting of quadrilateral elements. In contrast, in the present work an unstructured mesh consisting of triangular elements is used. However, this should not alleviate the problem of mesh distortion, since the deformation measure is still based on the deformation gradient. Void regions should give the same response, independent of the element type used.

When looking at computational costs, topology optimization based on nonlinear analysis is much more expensive than topology optimization based on linear analysis. The computation times for the examples presented in this chapter are in the order of minutes for the linear designs and in the order

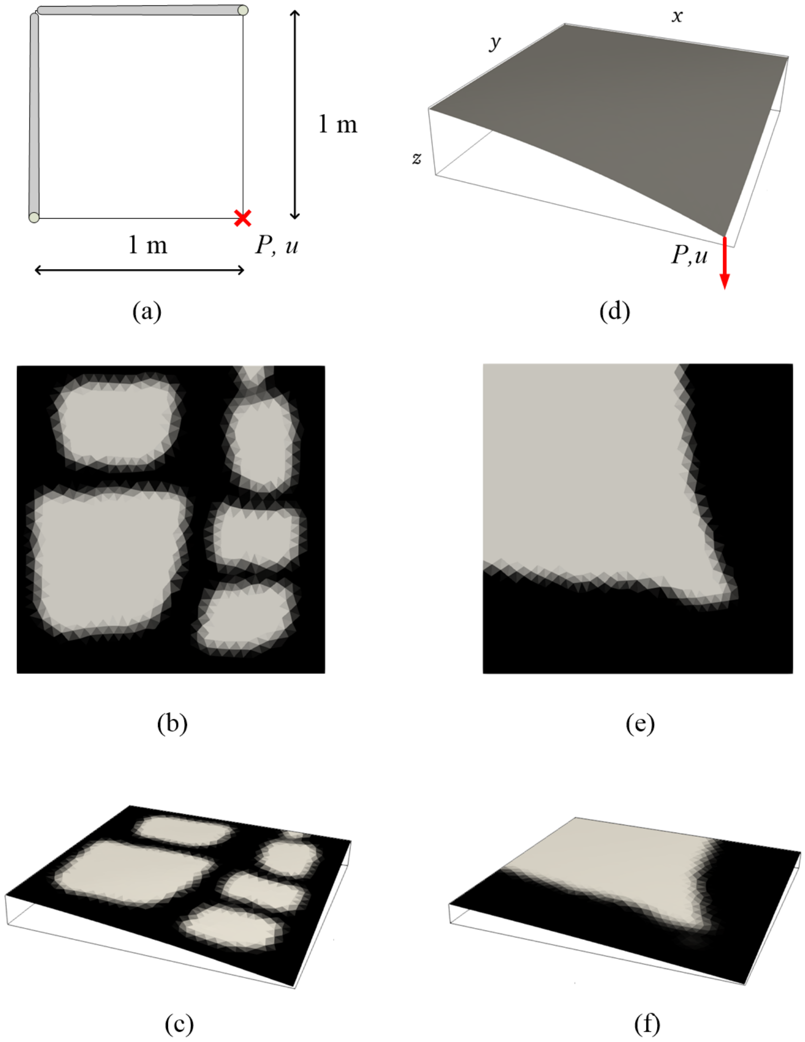

Figure 5.6: Topology optimization problem of the hinged square plate loaded out of plane. At the hinges the Dirichlet boundary condition $u_x = u_y = u_z = 0$ is applied. Displacements are not scaled. $P = 3\,\mathrm{N}$, $V^* = 0.5$, $n_{\mathrm{el}} = 2344$, $E = 200\,\mathrm{MPa}$, $\nu = 0$ and $h = 0.01\,\mathrm{m}$. (a) Design domain. (b) Optimal design obtained using linear analysis. (c) Deformed configuration of the linear design, $u = 0.11\,\mathrm{m}$. (d) Deformed configuration of the homogeneous initial design, $u = 0.24\,\mathrm{m}$. (e) Optimal design obtained using nonlinear analysis. (f) Deformed configuration of the nonlinear design, $u = 0.068\,\mathrm{m}$.

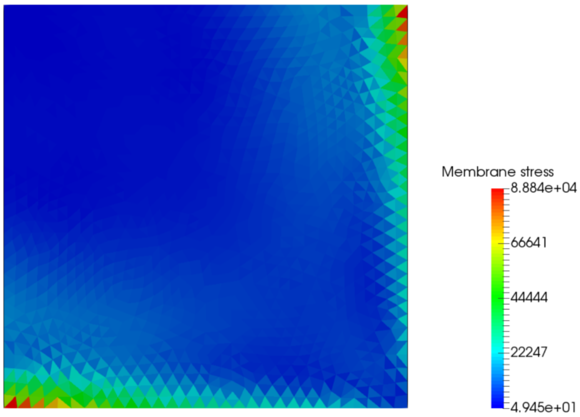

(a) Membrane von Mises stress of the initial homogeneous design based on the nonlinear model.

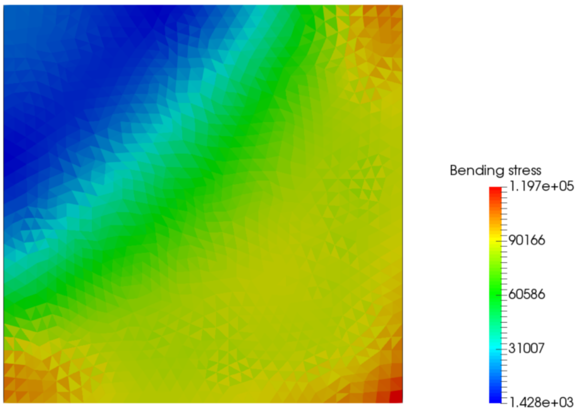

(b) Bending von Mises stress of the initial homogeneous design based on the nonlinear model.

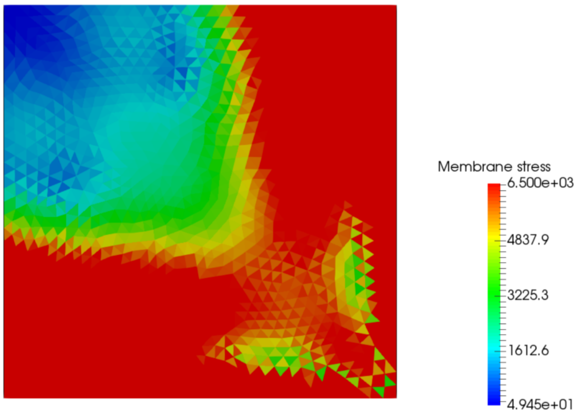

(c) Membrane von Mises stress of the initial homogeneous design based on the nonlinear model with a lower maximum value of the colormap.

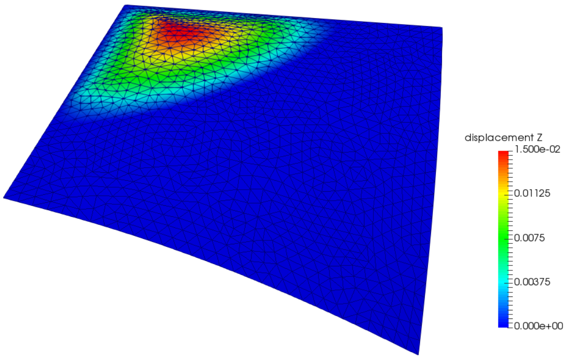

(d) Deformed configuration of the nonlinear design during design iteration 4. Displacements are scaled by a factor 3. The upward displaced area consists of intermediate density elements.

Figure 5.7: Von Mises stresses in the initial design of the hinged square plate calculated using the nonlinear model. In contrast to the stresses calculated using the linear model, the membrane (a) and bending stresses (b) are neither zero nor constant. The membrane stress field in (c) resembles the density field of the nonlinear design in Figure 5.6e. The upward displacement of the plate in (d) is only observed in the nonlinear model.

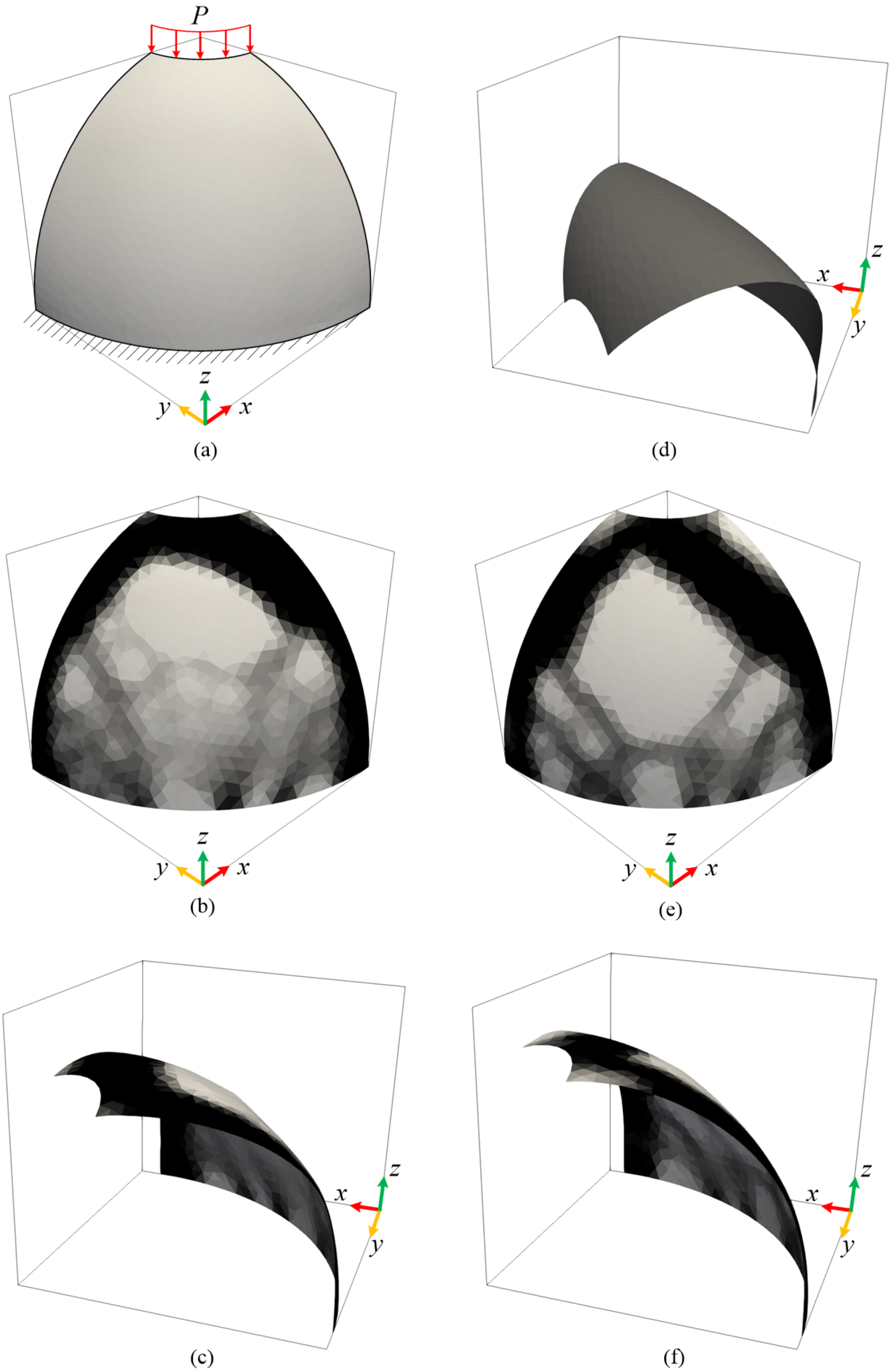

(a) (d)

(b) (e)

(c) (f)

Figure 5.8: Topology optimization problem of the spherical shell. Displacements are not scaled. The radius of the sphere in 10 m and the radius hole in the top is 3 m. The shell is fixed at the bottom: $u_x = u_y = u_z = \varphi = 0$ and a total force of $P = 2\,\mathrm{kN}$ is applied at the top. $V^* = 0.5$, $n_{\mathrm{el}} = 1356$, $E = 200\,\mathrm{MPa}$, $\nu = 0$ and $h = 0.1\,\mathrm{m}$. (a) Design domain. (b) Optimal design obtained using linear analysis. (c) Deformed configuration of the linear design. (d) Deformed configuration of the homogeneous initial design. (e) Optimal design obtained using nonlinear analysis. (f) Deformed configuration of the nonlinear design.

of hours for the nonlinear designs. In addition, shell problems are much more expensive than 2D problems. Because the number of degrees of freedom per element is doubled, the computation time is increased by a factor $2^3 = 8$ approximately. Finally, for all examples it holds that when the load is decreased, the differences between the linear and nonlinear designs also decrease.

6

OUTLOOK FOR DESIGNING STRUCTURES FOLLOWING PRESCRIBED EQUILIBRIUM PATHS

So far, a method has been presented to maximize the stiffness of structures. However, for some structures it is more important to control the equilibrium path, such as in MEMS and body supports as presented in Chapter 1. This is particularly interesting when the equilibrium path contains multiple stable equilibrium states. In this chapter a problem formulation will be presented to design such structures using topology optimization.

6.1 PROBLEM FORMULATION

The goal is to design a structure of which a specified degree of freedom follows a prescribed equilibrium path. The objective function can be formulated as the area between the target path and the path of an intermediate design, as illustrated in Figure 6.1. Since the equilibrium path is obtained via numerical analysis, it is not continuous but it consists of several discrete points (increments). Also, we want to prevent that positive and negative areas cancel each other out and the objective function has to be normalized. This leads to the following (smooth) objective function:

$$f = \sum_{k=1}^{n_{\text{incr}}} w_k \frac{(u_k - u_k^{\text{target}})^2}{(u_k^{\text{target}})^2}. \tag{6.1}$$

The weight factor w_k can be used to force the equilibrium path to pass through a specified point k.

In advance, the minimum value of the objective function is already known, namely, it is zero. This also means that the optimization problem has most likely no unique solution and a multitude of designs will be able to satisfy the criterion. The obtained design will follow the prescribed equilibrium path, but that does not mean it is able to transfer forces. To prevent this problem, the additional requirement is introduced that the design also has to pass through the prescribed points when two separate counter load cases are applied (in a 2D problem). One against the output direction and one perpendicular to the output direction of the specified degree of freedom. In this way, the mechanism will be stiffer and be able to transfer forces [44]. The improved objective function is

$$f = \sum_{m=0}^{2} \alpha_m \sum_{k=1}^{n_{\text{incr}}} w_k \frac{(u_k - u_k^{\text{target}})^2}{(u_k^{\text{target}})^2}, \tag{6.2}$$

were α_m is another weight factor. For $m = 0$ a counter force of zero is applied, for $m = 1$ the counter force acts against the output direction and for $m = 2$ the counter force is applied perpendicular to the

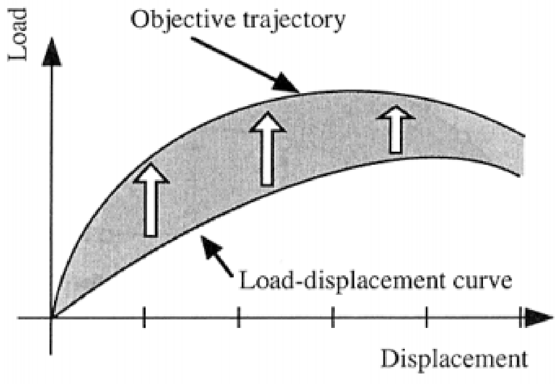

Figure 6.1: The objective function is the area between the target path and the path of an intermediate design [45].

output direction. This means that three separate nonlinear analyses have to be performed for every objective function evaluation, which makes it an expensive procedure. If the structure must have multiple stable equilibrium states, the arc-length control strategy implemented in Chapter 3 can be used to traverse these equilibrium paths.

One might wonder why the area is used in the objective function and why it is not imposed as a constraint. Since this constraint is extremely complex, the optimizer would spend a lot of effort on satisfying the constraint, and there would be little room for minimizing the objective function. Also, including the area in the objective function is less strict than defining it as a constraint. One could however relax on the constraint by defining an upper and lower limit of the area.

6.2 ADJOINT SENSITIVITIES

The sensitivity for element e is the derivative of the objective function f in Equation 6.2 with respect to the density of that element:

$$\frac{\partial f}{\partial \rho_e} = \sum_{m=0}^{2} \alpha_m \sum_{k=1}^{n_{\text{incr}}} 2w_k \frac{u_k - u_k^{\text{target}}}{(u_k^{\text{target}})^2} \frac{\partial u_k}{\partial \rho_e}. \tag{6.3}$$

Note that the state sensitivity $\partial u_k / \partial \rho_e$ appears in this expression. To simplify notation, from now on it is assumed that we want to find the sensitivity for point k on the equilibrium path, so this index is omitted. At the same time we assume that the equilibrium path is prescribed for the i'th degree of freedom. The displacement of degree of freedom i can be expressed as

$$u_i = \mathbf{l}^\top \mathbf{u}, \tag{6.4}$$

where $\mathbf{l}$ is the selection vector which has a value of one at entry i, and a value of zero everywhere else. The sensitivity of the displacement u_i with respect to the density of element e is

$$\frac{\partial u_i}{\partial \rho_e} = \mathbf{l}^\top \frac{\partial \mathbf{u}}{\partial \rho_e}. \tag{6.5}$$

This expression is similar to Equation 5.10, so the adjoint sensitivities are derived in the same way as in Section 5.3.1. In conclusion we can say that the state sensitivity of a specified degree of freedom i is

$$\frac{\partial u_i}{\partial \rho_e} = \boldsymbol{\mu}^\top \frac{\partial \mathbf{r}}{\partial \rho_e}, \tag{6.6}$$

where $\partial \mathbf{r}/\partial \rho_e$ can be computed using Equation 5.16 and $\boldsymbol{\mu}$ using

$$\boldsymbol{\mu} = \mathbf{K}^{-1}\mathbf{l}. \tag{6.7}$$

The state sensitivity can be substituted in Equation 6.3 to obtain the design sensitivity.

6.3 DESIGN CHALLENGES

Beside the challenges that are inherent to end-compliance minimization, there are more difficulties that come along with tracing prescribed equilibrium paths. They are enumerated in [46] and the most important difficulties are summarized below.

1. The nonlinear behavior of the (intermediate) designs might be even more complex than the nonlinearities dealt with in Chapters 3 and 5. Sharp turns and loopbacks can appear in the unstable regions of the equilibrium path. This complex behavior will occur in very localized areas of the mesh. Furthermore, the parameters of the arc-length control strategy have to be tuned automatically every design iteration.

2. The designer must perform several iterations in finding the right problem formulation. For example, finding the right weight functions can be difficult. Therefore, the design process is not fully automated and one of the biggest benefits of topology optimization is lost.

3. Several load cases are required for a good problem formulation. This makes the procedure very computationally expensive.

4. The most difficult task for the optimizer is to generate a design that exhibits snap-through behavior from an initial, uniformly distributed intermediate density design that does not. Therefore, an other approach for defining initial conditions should be developed.

5. If snap-through behavior is desired, there may be several different symmetric or asymmetric modes that cause this behavior. Besides, it may not be clear if antisymmetric modes develop because these modes are preferable or because the numerical computations have perturbed the design slightly from its symmetric case.

6. The design space will be less convex than for end-compliance minimization problems. Therefore, there is a bigger chance that the global optimum will not be found.

It can therefore be concluded that it is extremely difficult to design a structure that follows a prescribed equilibrium path.

7

CONCLUSIONS AND RECOMMENDATIONS

7.1 CONCLUSIONS

The aim of this work was to develop and implement the numerical tools required for topology optimization of geometrically nonlinear structures. For the three main goals the following conclusions can be drawn:

1. The Newton-Raphson incremental-iterative procedure in combination with arc-length control was implemented. This was done using the so called unified approach, which makes it possible to use any desired control strategy. This approach is very general and a different control strategy only requires a different expression for the iterative load. The highly nonlinear problem of the hinged cylindrical roof was analyzed and the results found are the same as the results obtained in literature by other authors.

2. It was investigated whether load dependent Ritz vectors can be used to create a reduced-order model, to decrease the computational costs of nonlinear analyses. It was demonstrated that in general a full basis cannot be constructed and therefore the reduced model is unable to approximate the displacement field in nonlinear static problems sufficiently.

3. The end-compliance minimization problem was implemented to design stiff geometrically nonlinear structures. By means of examples it was demonstrated that in most cases, especially for shell structures, this led to designs which perform better than designs obtained using topology optimization based on linear analysis. This is especially the case when large loads are applied. However, for very large loads the optimization process was not able to converge due to mesh distortion, and for very thin shells the optimization process was not able to converge due to an ill-conditioned tangent stiffness matrix.

Lastly, an outlook for the design of structures following a prescribed equilibrium path was provided. The present work was developed with this application in mind, which is why several important features, such as the arc-length control strategy and the sensitivities can be used. It is however more challenging than designing for stiffness and, in addition, the computation time is much longer, making the need of a reduction method even bigger.

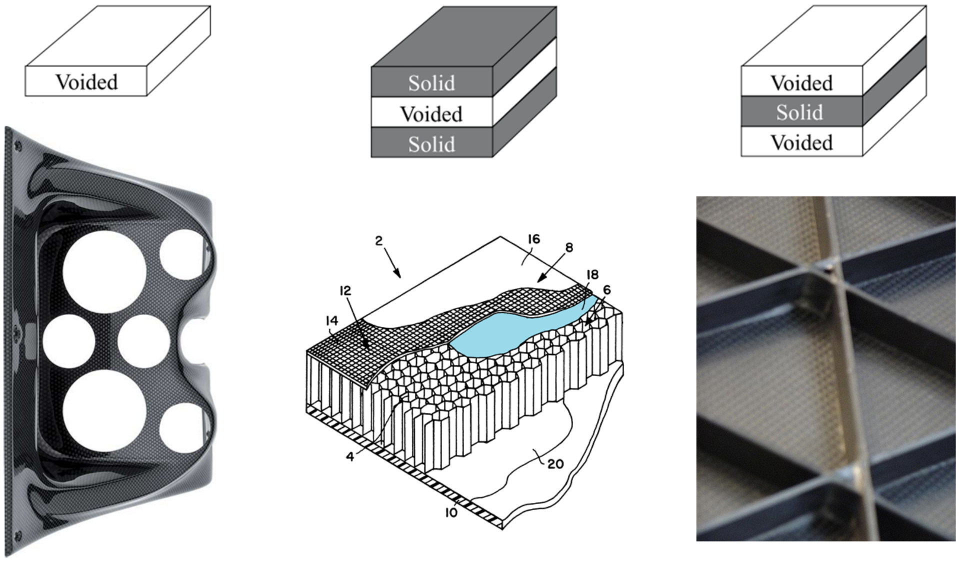

(a) (b) (c)

Figure 7.1: Examples of lamina sequences in multi-layered shells. (a) In the present work through-the-thickness holes are created in single-layered shells. (b) The outer layers of a sandwich panel are always kept solid. This allows for core design. (c) The middle layer is kept solid. This allows for rib design.

7.2 RECOMMENDATIONS

Various aspects of this work can be improved and features can be added. The most interesting ones are discussed in this section.

7.2.1 MULTI-LAYERED SHELLS

The application of topology optimization on shell structures has not received the same amount of attention as other fields in topology optimization. This is partly due to the fact that the essence of topology optimization is the ability to introduce holes in a structure. For the majority of engineering shell structures (fuselages, wings, ship hauls, turbine blades, etc.) it is not viable to introduce holes because of aerodynamic considerations [43]. The topology optimization of single-layered shells in the present work can be extended to multi-layered shells. This allows to keep some layers solid, while other layers can be designed freely. A very useful and practical application is core and rib design of sandwich panels, see Figure 7.1

7.2.2 SIZING OPTIMIZATION

In addition to density based topology optimization of shells, one could also look into sizing optimization. Here, the thickness instead of the density of each element is chosen as design variable. If the minimum thickness h_{min} is unequal to zero, this is called sizing optimization. If the minimum thickness is close to zero, it is a combination of sizing and topology optimization, since we have the ability to create holes. Just like the density, the thickness can never completely become zero, because this results in a singular stiffness matrix. In contrast to the density, the thickness does not have to be penalized, since intermediate thicknesses are allowed. However, since the bending stiffness scales with the thickness to the third power, it is penalized implicitly.

Similar to density based topology optimization, it is not desired to change the thickness in the constitutive matrix directly. We rather scale the tangent stiffness matrix and internal force vector separately. This is more complicated than for density based optimization, because not all terms scale with the same factor. The membrane stiffness scales linearly with the density, while the bending stiffness scales with the power three. The scaled element tangent stiffness matrix should therefore become:

$$\mathbf{K}_e = \begin{bmatrix} h\,\mathbf{K}_e^{\mathrm{mm}} & h^2\,\mathbf{K}_e^{\mathrm{mb}} \\ h^2\,\mathbf{K}_e^{\mathrm{mb}} & h^3\,\mathbf{K}_e^{\mathrm{bb}} \end{bmatrix} \tag{7.1}$$

where $\mathbf{K}_e^{\mathrm{mm}}$ represents the membrane stiffness and $\mathbf{K}_e^{\mathrm{bb}}$ the bending stiffness for unit thickness. $\mathbf{K}_e^{\mathrm{mb}}$ represents the coupling between in-plane and out-of-plane behavior for unit thickness and is zero for symmetric layered shells. The corresponding degrees of freedom in the internal force vector should be scaled accordingly.

7.2.3 OTHER RECOMMENDATIONS

Other features could be added, to improve the method presented in this work.

- The nonlinear analysis can be extended to be able to solve buckling problems. A bifurcation point is present when one of the eigenvalues of the tangent stiffness matrix becomes zero. Since it is very expensive to compute eigenvalues, a better approach is to monitor the pivots during the factorization. As soon as a pivot becomes zero, there is a zero eigenvalue and a bifurcation point is encountered. Subsequently, the corresponding eigenmode can be computed to steer the analysis to a certain branch of the equilibrium path.

- One of the existing reduction methods presented in Section 4.1 can be implemented to speed up the computations. Prediction and correction vectors (possibly in combination with eigenvectors) should yield the best result.

- The problem of mesh distortion can be prevented with one of the approaches discussed in Section 5.2. Preferably, either Element Deformation Scaling or the additive hyperelasticity technique is implemented, for the best results.

- The optimization process in this work is terminated based on the relative change in the objective function value. Since this is not a very good criterion, the process is continued manually for a fixed number of iterations. A better approach would be to terminate the process based on KKT-conditions [42].

A

ELEMENT STIFFNESS MATRICES

In this appendix the material and geometric stiffness matrices are derived for the elements used in this work. They are based on a Total Lagrange formulation.

A.1 NONLINEAR 2D TRUSS ELEMENT

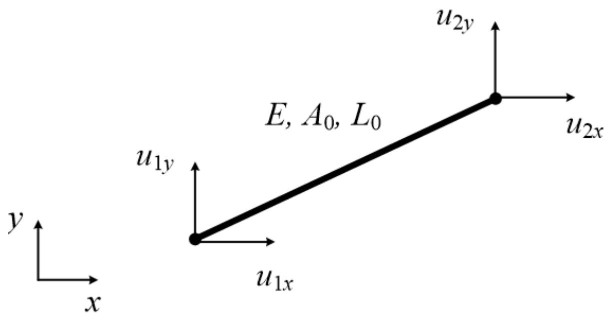

Figure A.1: Nonlinear 2D truss element.

The nonlinear 2D truss element is shown in Figure A.1. It has four degrees of freedom. The relation between the Green-Lagrange strain and displacements is

$$\varepsilon(\mathbf{u}) = \mathbf{B}_0\,\mathbf{u} + \tfrac{1}{2}\mathbf{u}^\top \mathbf{B}_1\,\mathbf{u} \tag{A.1}$$

where

$$\mathbf{B}_0 = \frac{1}{L_0}\begin{bmatrix} -1 & 0 & 1 & 0 \end{bmatrix}, \qquad \mathbf{B}_1 = \frac{1}{L_0^2}\begin{bmatrix} 1 & 0 & -1 & 0 \\ 0 & 1 & 0 & -1 \\ -1 & 0 & 1 & 0 \\ 0 & -1 & 0 & 1 \end{bmatrix} \tag{A.2}$$

are constant and linear strain-displacement matrices respectively and L_0 is the undeformed length. The total strain-displacement matrix is

$$\mathbf{B} = \mathbf{B}_0 + \mathbf{u}^\top \mathbf{B}_1 \tag{A.3}$$

The material stiffness matrix is

$$\mathbf{K}_\mathrm{M} = \int_{V_0} \mathbf{B}^\top \mathbf{D}\,\mathbf{B}\,\mathrm{d}V_0 = E A_0 L_0\,\mathbf{B}^\top \mathbf{B} \tag{A.4}$$

and the geometric stiffness matrix is

$$\mathbf{K}_{\mathrm{G}} = \int_{V_0} \frac{\partial^2 \varepsilon_k}{\partial u_i \partial u_j} \sigma_k \, \mathrm{d}V_0 = A_0 L_0 \sigma \, \mathbf{B}_1 \tag{A.5}$$

where E is the Young's modulus, A_0 the undeformed cross-sectional area, V_0 the undeformed volume and σ the second Piola-Kirchhoff stress.

A.2 NONLINEAR 3D TRIANGULAR MEMBRANE ELEMENT

The consistent tangent stiffness matrix of the shell element used in the present work has contributions of both membrane stresses and bending stresses. However, setting up this consistent tangent is very computationally expensive. Therefore, an inconsistent tangent is used where the contributions of the bending stresses in the geometric stiffness matrix are neglected. This approach results in slightly more iterations during the nonlinear analysis, but the overall computation time is much shorter. For this reason, the geometric stiffness matrix of the 3D triangular membrane element is derived in this section. For a more extensive description of the element, the reader is referred to [7].

TRIANGULAR COORDINATES

The triangular element is shown in the xy-plane in Figure A.2. The locations of the nodes and the corresponding nine degrees of freedom are defined in Cartesian coordinates: (x_i, y_i, z_i) and (u_{ix}, u_{iy}, u_{iz}), $i = 1,2,3$, respectively. The T3-element is an isoparametric element, and triangular coordinates ζ_i, $i = 1,2,3$, will be used for the linear interpolation. The mapping between Cartesian and triangular coordinates is as follows

$$\begin{bmatrix} 1 \\ x \\ y \end{bmatrix} = \begin{bmatrix} 1 & 1 & 1 \\ x_1 & x_2 & x_3 \\ y_1 & y_2 & y_3 \end{bmatrix} \begin{bmatrix} \zeta_1 \\ \zeta_2 \\ \zeta_3 \end{bmatrix} \tag{A.6}$$

The first equation says that the sum of the three coordinates is one. The next two express x and y linearly in triangular coordinates. Inverting this relation gives

$$\begin{bmatrix} \zeta_1 \\ \zeta_2 \\ \zeta_3 \end{bmatrix} = \frac{1}{2A_0} \begin{bmatrix} 2A_1 & y_{23} & x_{32} \\ 2A_2 & y_{31} & x_{13} \\ 2A_3 & y_{12} & x_{21} \end{bmatrix} \begin{bmatrix} 1 \\ x \\ y \end{bmatrix} \tag{A.7}$$

where $x_{jk} = x_j - x_k$, $y_{jk} = y_j - y_k$, A_0 is the area of the element and A_i is the area between the corners opposite of node i and the origin of the xy-system.

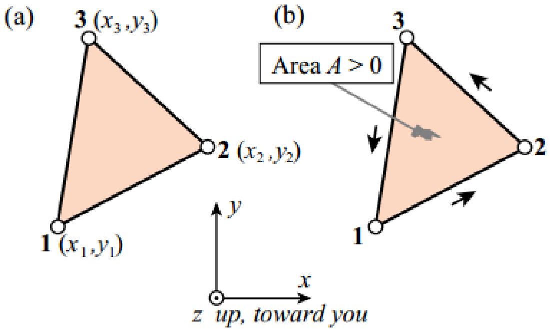

Figure A.2: Three-node nonlinear triangular membrane element (T3).

STRAIN-DISPLACEMENT RELATION

The displacement vector is defined as

$$\mathbf{u} = \begin{bmatrix} u_{1x} & u_{1y} & u_{1z} & u_{2x} & u_{2y} & u_{2z} & u_{3x} & u_{3y} & u_{3z} \end{bmatrix}^\top \tag{A.8}$$

The continuous displacement field is obtained by interpolating the nodal displacement. For the x-direction, this gives

$$u_x = \zeta_1 u_{1x} + \zeta_2 u_{2x} + \zeta_3 u_{3x} \tag{A.9}$$

The Green-Lagrange strain vector contains the membrane strains.

$$\boldsymbol{\varepsilon} = \begin{bmatrix} \varepsilon_{xx} \\ \varepsilon_{yy} \\ \varepsilon_{xy} \end{bmatrix} = \frac{1}{2} \begin{bmatrix} u_{x,x} + u_{x,x} + u_{x,x}^2 + u_{y,x}^2 + u_{z,x}^2 \\ u_{y,y} + u_{y,y} + u_{x,y}^2 + u_{y,y}^2 + u_{z,y}^2 \\ u_{x,y} + u_{y,x} + u_{x,x}u_{x,y} + u_{y,x}u_{y,y} + u_{z,x}u_{z,y} \end{bmatrix} \tag{A.10}$$

Next, the terms in the Green-Lagrange strain vector can be elaborated further using Equation A.7 and Equation A.9. Since ζ_i is a function of x_i, the chain rule is applied. The first term yields

$$\begin{aligned} u_{x,x} &= \frac{\partial u_x}{\partial \zeta_1}\frac{\partial \zeta_1}{\partial x} + \frac{\partial u_x}{\partial \zeta_2}\frac{\partial \zeta_2}{\partial x} + \frac{\partial u_x}{\partial \zeta_3}\frac{\partial \zeta_3}{\partial x} \\ &= u_{1x}\left(\frac{1}{2A_0}y_{23}\right) + u_{2x}\left(\frac{1}{2A_0}y_{31}\right) + u_{3x}\left(\frac{1}{2A_0}y_{12}\right) \\ &= \frac{1}{2A_0}\left(u_{1x}y_{23} + u_{2x}y_{31} + u_{3x}y_{12}\right) \end{aligned} \tag{A.11}$$

The other terms are derived in the same fashion.

Constitutive model

The second Piola-Kirchhoff stress is related to the Green-Lagrange strain by the constitutive matrix **D**.

$$\boldsymbol{\sigma} = \mathbf{D}\boldsymbol{\varepsilon} \qquad \text{where} \qquad \mathbf{D} = \frac{E}{1-\nu^2}\begin{bmatrix} 1 & \nu & 0 \\ \nu & 1 & 0 \\ 0 & 0 & \frac{1-\nu}{2} \end{bmatrix} \tag{A.12}$$

where E is the Young's modulus and ν the Poisson's ratio.

Material stiffness matrix

Using Equations A.9 and A.10 the strain-displacement matrix can be expressed as

$$\mathbf{B} = \begin{bmatrix} y_{23} & 0 & 0 & y_{31} & 0 & 0 & y_{12} & 0 & 0 \\ 0 & x_{32} & 0 & 0 & x_{13} & 0 & 0 & x_{21} & 0 \\ x_{32} & y_{23} & 0 & x_{13} & y_{31} & 0 & x_{21} & y_{12} & 0 \end{bmatrix} \tag{A.13}$$

The material stiffness matrix for the triangular element becomes

$$\mathbf{K}_{\mathrm{M}} = \int_{V_0} \mathbf{B}^\top \mathbf{D}\mathbf{B}\, \mathrm{d}V_0 = A_0 h_0 \mathbf{B}^\top \mathbf{D}\mathbf{B} \tag{A.14}$$

where V_0, A_0 and h_0 are respectively the volume, area and thickness of the element in the undeformed configuration.

Geometric stiffness matrix

As derived in Section 2.2, the geometric stiffness matrix is

$$K_{\mathrm{G}_{ij}} = \int_{V_0} \frac{\partial^2 \varepsilon_k}{\partial u_i \partial u_j}\sigma_k \, \mathrm{d}V_0 \qquad i,j = 1,2,\ldots,9 \quad \text{and} \quad k = 1,2,3 \tag{A.15}$$

Since the strain is derived twice with respect to the displacements, all linear terms vanish. The first quadratic term in $\boldsymbol{\varepsilon}$ is the square of Equation A.11.

$$u_{x,x}^2 = \frac{1}{2}\cdot\frac{1}{4A_0^2}\left(u_{1x}y_{23} + u_{2x}y_{31} + u_{3x}y_{12}\right)^2 \tag{A.16}$$

The first derivative yields

$$\frac{\partial u_{x,x}^2}{\partial u_1} = \frac{1}{4A_0^2}\left(u_{1x}y_{23} + u_{2x}y_{31} + u_{3x}y_{12}\right)y_{23} \tag{A.17}$$

and subsequently the second derivative yields

$$\frac{\partial^2 u_{x,x}^2}{\partial u_1^2} = \frac{1}{4A_0^2}y_{23}^2 \tag{A.18}$$

The other terms are derived in the same fashion. This leads to the following geometric stiffness matrix

$$\mathbf{K}_\mathrm{G} = \begin{bmatrix} K_{\mathrm{G}_{11}} & 0 & 0 & K_{\mathrm{G}_{14}} & 0 & 0 & K_{\mathrm{G}_{17}} & 0 & 0 \\ & K_{\mathrm{G}_{22}} & 0 & 0 & K_{\mathrm{G}_{25}} & 0 & 0 & K_{\mathrm{G}_{28}} & 0 \\ & & K_{\mathrm{G}_{33}} & 0 & 0 & K_{\mathrm{G}_{36}} & 0 & 0 & K_{\mathrm{G}_{39}} \\ & & & K_{\mathrm{G}_{44}} & 0 & 0 & K_{\mathrm{G}_{47}} & 0 & 0 \\ & & & & K_{\mathrm{G}_{55}} & 0 & 0 & K_{\mathrm{G}_{58}} & 0 \\ & & & & & K_{\mathrm{G}_{66}} & 0 & 0 & K_{\mathrm{G}_{69}} \\ & & & & & & K_{\mathrm{G}_{77}} & 0 & 0 \\ & \text{sym.} & & & & & & K_{\mathrm{G}_{88}} & 0 \\ & & & & & & & & K_{\mathrm{G}_{99}} \end{bmatrix} \tag{A.19}$$

consisting of six different terms

$$\begin{aligned}
K_{\mathrm{G}_{11}} = K_{\mathrm{G}_{22}} = K_{\mathrm{G}_{33}} &= \frac{h_0}{4A_0}\left[y_{23}^2 \quad x_{32}^2 \quad x_{32}y_{23}\right]\boldsymbol{\sigma} \\
K_{\mathrm{G}_{44}} = K_{\mathrm{G}_{55}} = K_{\mathrm{G}_{66}} &= \frac{h_0}{4A_0}\left[y_{31}^2 \quad x_{13}^2 \quad x_{13}y_{31}\right]\boldsymbol{\sigma} \\
K_{\mathrm{G}_{77}} = K_{\mathrm{G}_{88}} = K_{\mathrm{G}_{99}} &= \frac{h_0}{4A_0}\left[y_{12}^2 \quad x_{21}^2 \quad x_{21}y_{12}\right]\boldsymbol{\sigma} \\
K_{\mathrm{G}_{14}} = K_{\mathrm{G}_{25}} = K_{\mathrm{G}_{36}} &= \frac{h_0}{4A_0}\left[y_{23}y_{31} \quad x_{13}x_{32} \quad \tfrac{1}{2}(x_{13}y_{23} + x_{32}y_{31})\right]\boldsymbol{\sigma} \\
K_{\mathrm{G}_{17}} = K_{\mathrm{G}_{28}} = K_{\mathrm{G}_{39}} &= \frac{h_0}{4A_0}\left[y_{12}y_{23} \quad x_{21}x_{32} \quad \tfrac{1}{2}(x_{21}y_{23} + x_{32}y_{12})\right]\boldsymbol{\sigma} \\
K_{\mathrm{G}_{47}} = K_{\mathrm{G}_{58}} = K_{\mathrm{G}_{69}} &= \frac{h_0}{4A_0}\left[y_{12}y_{31} \quad x_{13}x_{21} \quad \tfrac{1}{2}(x_{13}y_{12} + x_{21}y_{31})\right]\boldsymbol{\sigma}
\end{aligned} \tag{A.20}$$

BIBLIOGRAPHY

[1] R. Kemmler, A. Lipka, and E. Ramm, *Large deformations and stability in topology optimization,* Structural and Multidisciplinary Optimization **30**, 459 (2005).

[2] T. Zegard and G. H. Paulino, *Bridging topology optimization and additive manufacturing,* Structural and Multidisciplinary Optimization **53**, 175 (2016).

[3] G. Radaelli and W. Van de Sande, *Shell-mech symposium,* (2016).

[4] Nava, *Difference between fea and cfd,* (2017).

[5] Y.-J. Yang, B.-T. Liao, and W.-C. Kuo, *A novel 2× 2 mems optical switch using the split cross-bar design,* Journal of Micromechanics and Microengineering **17**, 875 (2007).

[6] C. Felippa, *Nonlinear Finite Element Methods*, Vol. V (2016) Chap. 29.

[7] T. Smit, *Modeling of non-rigid origami*, Master's thesis (2017).

[8] F. Van Keulen, *Refined triangular plate and shell elements*, Ph.D. thesis (1993).

[9] F. Van Keulen and J. Booij, *Refined consistent formulation of a curved triangular finite rotation shell element,* International journal for numerical methods in engineering **39**, 2803 (1996).

[10] M. Crisfield and V. Ciampi, *Non-linear Finite Element Analysis of Solids and Structures Vol. 1*, Vol. 32 (1997) pp. 586–587.

[11] T. Bruns, O. Sigmund, and D. A. Tortorelli, *Numerical methods for the topology optimization of structures that exhibit snap-through,* International Journal for Numerical Methods in Engineering **55**, 1215 (2002).

[12] J.-L. Batoz and G. Dhatt, *Incremental displacement algorithms for nonlinear problems,* International Journal for Numerical Methods in Engineering **14**, 1262 (1979).

[13] D. C. Lay, *Linear algebra and its applications* (Addison-Wesley, 2002).

[14] R. de Borst and L. J. Sluys, *Computational Methods in Nonlinear Solid Mechanics* (2015).

[15] M. A. Crisfield, *A fast incremental/iterative solution procedure that handles 'snap-through',* Computers & Structures **13**, 55 (1981).

[16] S. E. Leon, G. H. Paulino, A. Pereira, I. F. Menezes, and E. N. Lages, *A unified library of nonlinear solution schemes,* Applied Mechanics Reviews **64**, 040803 (2011).

[17] B. Haugen, *Numerical examples of thin shell analysis (chapters 6-8),* (2013).

[18] A. Quarteroni, A. Manzoni, and F. Negri, *Reduced Basis Methods for Partial Differential Equations: An Introduction*, UNITEXT (Springer International Publishing, 2015).

[19] A. K. Noor and J. M. Peters, *Multiple-parameter reduced basis technique for bifurcation and post-buckling analyses of composite plates,* International Journal for Numerical Methods in Engineering **19**, 1783 (1983).

[20] A. K. Noor and J. M. Peters, *Tracing post-limit-point paths with reduced basis technique,* Computer Methods in Applied Mechanics and Engineering **28**, 217 (1981).

[21] A. K. Noor and J. M. Peters, *Bifurcation and post-buckling analysis of laminated composite plates via reduced basis technique,* Computer Methods in Applied Mechanics and Engineering **29**, 271 (1981).

[22] A. Chan and K. Hsiao, *Nonlinear analysis using a reduced number of variables,* Computer Methods in Applied Mechanics and Engineering **52**, 899 (1985).

[23] A. Safjan, *Nonlinear structural analysis via reduced basis technique,* Computers & structures **29**, 1055 (1988).

[24] D. A. Nagy and M. König, *Geometrically nonlinear finite element behaviour using buckling mode superposition,* Computer Methods in Applied Mechanics and Engineering **19**, 447 (1979).

[25] H. Gavin, *Mathematical properties of stiffness matrices,* (2006).

[26] E. L. Wilson, M.-W. Yuan, and J. M. Dickens, *Dynamic analysis by direct superposition of ritz vectors,* Earthquake Engineering & Structural Dynamics **10**, 813 (1982).

[27] T. Van der Linde, *Fast topology optimization for transient mechanical problems*, Master's thesis, TU Delft, Delft University of Technology (2016).

[28] W. Kanok-Nukulchai and S. Lin, *Nonlinear analysis using ritz vector reduced basis,* Computers & structures **44**, 117 (1992).

[29] K. D. Hjelmstad, *Fundamentals of structural mechanics* (Springer Science & Business Media, 2007).

[30] W. Ruchala, *Earthquake analysis of bridge systems by Ritz vectors* (1998).

[31] D. J. Rixen, *Numerical methods in Engineering Dynamics* (2014).

[32] P. A. Browne, *Topology optimization of linear elastic structures*, Ph.D. thesis, University of Bath (2013).

[33] J. D. Deaton and R. V. Grandhi, *A survey of structural and multidisciplinary continuum topology optimization: post 2000,* Structural and Multidisciplinary Optimization **49**, 1 (2014).

[34] O. Sigmund and J. Petersson, *Numerical instabilities in topology optimization: a survey on procedures dealing with checkerboards, mesh-dependencies and local minima,* Structural and Multidisciplinary Optimization **16**, 68 (1998).

[35] A. G. M. Michell, *Lviii. the limits of economy of material in frame-structures,* The London, Edinburgh, and Dublin Philosophical Magazine and Journal of Science **8**, 589 (1904).

[36] K. Svanberg, *The method of moving asymptotes: a new method for structural optimization,* International journal for numerical methods in engineering **24**, 359 (1987).

[37] M. E. Gurtin, *An introduction to continuum mechanics, volume 158 of mathematics in science and engineering,* (1981).

[38] N. P. van Dijk, M. Langelaar, and F. van Keulen, *Element deformation scaling for robust geometrically nonlinear analyses in topology optimization,* Structural and Multidisciplinary Optimization **50**, 537 (2014).

[39] G. H. Yoon and Y. Y. Kim, *Element connectivity parameterization for topology optimization of geometrically nonlinear structures,* International journal of solids and structures **42**, 1983 (2005).

[40] Y. Luo, M. Y. Wang, and Z. Kang, *Topology optimization of geometrically nonlinear structures based on an additive hyperelasticity technique,* Computer Methods in Applied Mechanics and Engineering **286**, 422 (2015).

[41] M. Langelaar, *Eng. optimization: Concept & applications,* (2015).

[42] P. W. Christensen and A. Klarbring, *An introduction to structural optimization*, Vol. 153 (Springer Science & Business Media, 2008).

[43] J. Stegmann and E. Lund, *Nonlinear topology optimization of layered shell structures,* Structural and Multidisciplinary Optimization **29**, 349 (2005).

[44] C. B. Pedersen, T. Buhl, and O. Sigmund, *Topology synthesis of large-displacement compliant mechanisms,* International Journal for numerical methods in engineering **50**, 2683 (2001).

[45] T. Sekimoto and H. Noguchi, *Homologous topology optimization in large displacement and buckling problems.* JSME International Journal Series A Solid Mechanics and Material Engineering **44**, 616 (2001).

[46] T. Bruns and O. Sigmund, *Toward the topology design of mechanisms that exhibit snap-through behavior,* Computer Methods in Applied Mechanics and Engineering **193**, 3973 (2004).